Strategies for realizing high-efficiency silicon heterojunction solar cells

Zhao, Yifeng; Procel, Paul; Han, Can; Cao, Liqi; Yang, Guangtao; Özkol, Engin; Alcañiz, Alba; Kovačević, Katarina; Limodio, Gianluca; Santbergen, Rudi

DOI
10.1016/j.solmat.2023.112413

Publication date
2023

Document Version
Final published version

Published in
Solar Energy Materials and Solar Cells

Solar Energy Materials & Solar Cells 258 (2023) 112413

Contents lists available at ScienceDirect

Solar Energy Materials and Solar Cells

journal homepage: www.elsevier.com/locate/solmat

Strategies for realizing high-efficiency silicon heterojunction solar cells

Yifeng Zhao [a,*], Paul Procel [a], Can Han [a], Liqi Cao [a], Guangtao Yang [a], Engin Özkol [a], Alba Alcañiz [a], Katarina Kovačević [a], Gianluca Limodio [a], Rudi Santbergen [a], Arno Smets [a], Arthur Weeber [a,b], Miro Zeman [a], Luana Mazzarella [a], Olindo Isabella [a]

[a] Photovoltaic Materials and Devices Group, Delft University of Technology, Delft, the Netherlands
[b] TNO Energy Transition, Solar Energy, Petten, the Netherlands

A B S T R A C T

Silicon heterojunction (SHJ) solar cells have achieved a record efficiency of 26.81% in a front/back-contacted (FBC) configuration. Moreover, thanks to their advantageous high V_{OC} and good infrared response, SHJ solar cells can be further combined with wide bandgap perovskite cells forming tandem devices to enable efficiencies well above 33%. In this study, we present strategies to realize high-efficiency SHJ solar cells through combined theoretical and experimental studies, starting from the optimization of Si-based thin-film layers to the implementation of electrodes with reduced indium and silver usage. Advanced opto-electrical simulations, which enable comprehensive theoretical understandings of the main physical mechanisms governing carriers' collection and light management, provide clear pathways for device designs and experimental optimizations. We present the fabricated FBC-SHJ solar cells in both monofacial and bifacial configurations with the best efficiencies of 24.18% and 23.25%, respectively. We point out that to achieve optimum device performance, the compositional materials should be holistically optimized and evaluated as part of the contact stacks with adjacent layers. As an outlook beyond the classical FBC-SHJ solar cell architecture, we propose various novel SHJ-based solar cell architectures. Their potential performance was assessed and compared via rigorous opto-electrical simulations and a maximal efficiency of 27.60% was simulated for FBC-SHJ solar cells featuring localized contacts.

1. Introduction

The photovoltaic industry is a technologically diverse market despite that different types of solar cells share the same basic working principle, i.e., the photovoltaic (PV) effect [1]. Nowadays, the commercial PV market is mainly shared by wafer-based crystalline silicon (c-Si) technologies and thin-film technologies. Thanks to the abundance of Si, processing maturity, high efficiency and long service time (over 25 years), c-Si technologies own around 95% of the global annual PV production in 2021 [2]. It is well-accepted that the continuously improved efficiency of solar cells (modules) and reduced manufacturing costs are strongly backing the success of the PV industry. Among different factors that promote the advancement of the PV industry, uninterrupted technological innovations are of great importance.

1.1. Evolution of c-Si PV technologies towards carrier-selective passivating contacts

Starting with the aluminium-doped back surface field (Al-BSF) solar cells, they feature simple architecture (see Fig. 1(a)) and were the main working horse of the PV industry in the past decades till 2013. However, mainly due to the full-area direct contact of metal and Si at the rear side, Al-BSF solar cells exhibit high recombination losses of photogenerated electrons and holes, thus limiting the open-circuit voltage (V_{OC}) to below 650 mV. In addition to the high parasitic absorption and non-optimum internal reflection at the rear side, the best Al-BSF solar cell has an efficiency of 20.29% [3]. Commercially, the Al-BSF cells exhibit around 20% efficiencies [4]. The recombination losses, especially at the rear side of Al-BSF cells, can be reduced by introducing a dielectric passivating layer between the Si and rear metal contact. This type of cell is referred to as the passivated emitter and rear cells (PERC) as first reported in 1989 [5] and in 2022 it possesses the largest portion of the market [6]. As seen from a typical commercial PERC solar cell sketched in Fig. 1(b), the rear side of typical PERC cell features point contacts together with heavily doped p^+ regions, while the non-contacted surface is covered by the layer stack such as AlO_x/SiN_y for suppressing the surface recombination and enhancing the internal reflectance [7,8]. PERC-based architectures (PER'X') such as passivated emitter rear locally diffused (PERL) (Fig. 1(c)) [9] and passivated emitter rear totally diffused (PERT) (Fig. 1(d)) [10] solar cells, featuring either locally- or fully-diffused boron-doped (B-doped) regions, respectively, are also industrial appealing [6]. Overall for the PER'X' family, a long-held record

* Corresponding author.
E-mail address: y.zhao-4@tudelft.nl (Y. Zhao).

https://doi.org/10.1016/j.solmat.2023.112413
Received 24 April 2023; Received in revised form 1 June 2023; Accepted 4 June 2023
Available online 11 June 2023

efficiency of 25% was achieved with a high V_{OC} of 706 mV back in 1999 [10–12]. In mass production till 2022, the PERC cells have efficiencies of about 24% [13].

For both Al-BSF and PER'X' solar cells, although diffused doping of wafer surfaces can partially reduce the recombinations by minimizing the concentration of minority carriers at the metal/Si interface, it also introduces significant Auger recombination, free carrier absorption (FCA), and bandgap narrowing that limit their efficiencies [14–17]. To alleviate, basically, the direct contact between the metal and silicon wafer, solar cells with carrier-selective passivating contacts (CSPCs) are developed. As the name suggests, stacks of thin-film layers are deposited on both sides of the wafer to passivate the surface defects of the wafer and selectively collect the photogenerated charge carriers. The prominent examples are low-thermal budget silicon heterojunction (SHJ) solar cells [18] and high-thermal budget tunnel-oxide passivating contacts (TOPCon) [19] or doped polysilicon (poly-Si) on oxide junction (POLO) [20] solar cells (see Fig. 1(e)–(g)). For SHJ and TOPCon solar cells, optimized thin (<10 nm) hydrogenated intrinsic amorphous silicon ((*i*) a-Si:H) layers and ultra-thin (<2 nm) silicon oxide (SiO_x) layers are utilized, respectively, to provide excellent chemical passivation of c-Si surfaces. Then, typically, doped a-Si:H or poly-Si layers, or their alloys with oxygen or carbon [21–33], are implemented to achieve carrier selectivity, respectively. SHJ solar cells have reached a record efficiency of 26.81% [34] with a high V_{OC} of 751.4 mV in a front/back-contacted (FBC) configuration, and 26.7% in an interdigitated back-contacted (IBC) architecture [35]. Till the end of 2022, the best TOPCon solar cell efficiency has reached 26.4% [36] and POLO-IBC demonstrated an efficiency of 26.1% [37]. Besides such record devices, in production lines till 2022, solar cells with CSPCs deliver efficiencies of around 25% [38,39].

These concepts of CSPCs entail the use of either doped a-Si:H or poly-Si layers which exhibit high parasitic absorption when placed on the illumination side of the solar cells. Alternatively, dopant-free transition metal oxides (TMOs), which are more transparent than the above-mentioned silicon-based layers, can mitigate this optical loss while providing sufficient carrier selectivity. Materials with high work function (WF), such as molybdenum oxide (MoO_x) [40–43], tungsten oxide (WO_x) [44,45] and vanadium oxide (VO_x) [46], can be used as hole transport layers (HTLs). Materials with low WF, such as lithium fluoride (LiF_x) [47], magnesium oxide (MgO_x) [48], magnesium fluoride (MgF_2) [49], titanium oxide (TiO_x) [50,51], or strontium fluoride (SrF_2) [52] can be used as electron transport layers (ETLs) [47,53]. In particular, in the Photovoltaic Materials and Devices (PVMD) group of Delft University of Technology, we recently demonstrated the promising use of MoO_x as the front HTL in SHJ solar cells with a certified record efficiency of 23.83% [54]. As sketched in Fig. 1(h) [55], researchers presented a 21.4%-efficient solar cell with dopant-free contacts on both sides, where MoO_x/ITO/Ag and ZnO/LiF_x/Al contact stacks are used for hole and electron collections, respectively. Besides, both unencapsulated SHJ solar cells and encapsulated modules endowed with MoO_x were reported to retain over 95% of their initial efficiencies after standard damp heat stability tests [56–58], demonstrating the promising viability of this technology. Nevertheless, additional research is required for further progressing TMO-based SHJ solar cells.

Overall, SHJ solar cell that holds the highest single-junction c-Si efficiency is one of the most promising c-Si technologies nowadays and it is predicted to own a 20% market share by 2032 [59]. Its application, together with high bandgap perovskite solar cells to reduce losses induced by spectral mismatch, is critical for reducing the levelized cost of electricity (LCOE) of PV power plants. Till May of 2023, two-terminal (2T), three-terminal (3T) and four-terminal (4T) perovskite/SHJ tandem solar cells have achieved remarkable efficiencies of 33.7% (area: 1.0035 cm^2), 29.56% (area: 24.5 cm^2), and 30.79% (area: 64 cm^2), respectively [60–62]. Challenges remain in scaling up and mitigating the instability of the perovskite subcells. Altogether, thanks to the substantial research progress made with perovskite/c-Si tandem solar cells [63–66], the momentum of continuous solar cell efficiency increment is secured.

1.2. A brief recap of the efficiency progression of SHJ solar cells

The SHJ with (*i*)a-Si:H layers, also initially known as 'Heterojunction with Intrinsic Thin-layer' (HIT) solar cell was first introduced by Panasonic (Sanyo) with an efficiency of 18.1%, significantly marking better V_{OC} and *FF* values at cell level than those achieved in similar c-Si solar cell architectures without the (*i*)a-Si:H passivating layer [18]. Apart from the continuous developments from Panasonic (Sanyo) that resulted in an efficiency of 23.7% with a 98-μm-thin wafer (area: 100.7 cm^2) in 2011 [71–76], the high-efficiency SHJ technology also attracted numerous research interests from universities, research institutes and companies worldwide [53,77–79], especially around the expiration period of 'core' SHJ patents [80]. Two years later, in 2013, Panasonic (Sanyo) improved the efficiency to 24.7% by reducing the interface recombination of (*i*)a-Si:H/c-Si together with minimizing the resistive losses in the solar cells [81]. In 2014, they realized another jump in

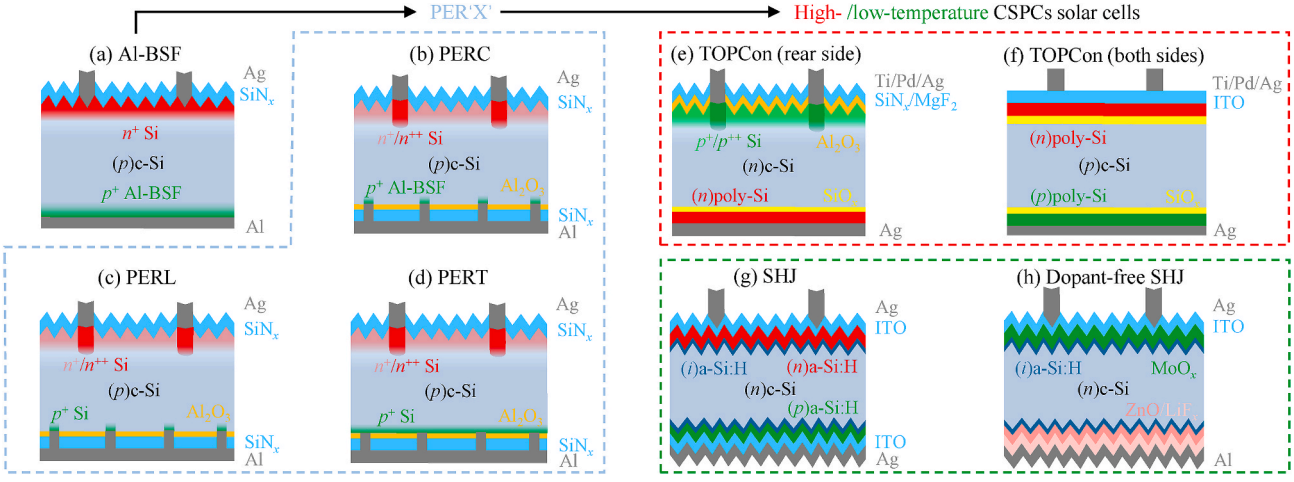

Fig. 1. Schematic representations of the evolution of c-Si PV technologies towards carrier-selective passivation contacts (CSPCs): a) Al-doped Back Surface Field (Al-BSF) solar cells [53]; b) Passivated Emitter and Rear Cells (PERC) [67]; c) Passivated Emitter and Rear Locally diffused cells (PERL) [68]; d) Passivated Emitter and Rear Totally diffused cells (PERT) [69]; e) Solar cell with a tunnel oxide passivating contact (TOPCon) on the rear side [19]; f) Solar cell with TOPCon on both sides [70]; g) Silicon heterojunction (SHJ) solar cells [69]; h) Dopant-free SHJ solar cells [55]. The presented structures are typical device designs that are adapted from their corresponding references.

efficiency to 25.6% by implementing an IBC configuration [82]. Nevertheless, soon after, FBC-SHJ solar cell fabricated by Kaneka reached an efficiency of 25.1%, which also focused on recombination mitigation at the (*i*)a-Si:H/c-Si interface [83]. In 2017, Kaneka achieved an efficiency of 26.7% for an IBC-SHJ solar cell [35], which was a long-held record efficiency for single-junction c-Si solar cells until November 2022. At that time, LONGi announced a record-breaking efficiency of 26.81% for an FBC-SHJ solar cell (area: 274.4 cm^2), which features a J_{SC} of 41.5 mA/cm^2, a V_{OC} of 751.4 mV, a *FF* of 86.07% [84]. The certified record efficiency progression of low-thermal budget SHJ solar cells since the first 'HIT' solar cell is illustrated in Fig. 2.

Such optimized opto-electrical performance of the SHJ solar cell must require a thorough theoretical understanding of device designs, experimental optimizations and careful processing. Tremendous efforts are being put internationally into the technology development and multi-gigawatt industrialization of SHJ solar cells and modules [53,59,77,78,85–90]. However, the increasing demand of raw materials such as silver and indium, which are critical to this PV technology, has triggered comprehensive studies on the growth perspectives of this PV technology, from both the industrialization and sustainability standpoints [59,90,91].

In this contribution, we present experimental efficiency improvements for FBC-SHJ solar cells from around 18% to above 24% at the laboratory scale by following the guidelines provided by our rigorous device, material and optical simulations. We here provide our experience as (i) a roadmap showing the progressively enhanced device *FF* guided by simulations, (ii) the optimized high-efficiency monofacial and bifacial solar cells featuring nc-Si:H-based and/or MoO_x-based contact stack, (iii) SHJ structures with less indium-based transparent conductive oxide (TCO) and silver consumption. Finally, based on numerical simulations, we present different innovative SHJ-based solar cell designs addressing advantages and drawbacks compared with state-of-art SHJ technology.

2. General experimental details

2.1. Fabrication of FBC-SHJ solar cells

For fabricating FBC-SHJ solar cells, we used 4-inch Topsil *n*-type double-side-polished float-zone (FZ) <100>-oriented c-Si wafers, which are 280 ± 20-μm-thick with resistivities of 3 ± 2 Ω·cm. Both sides of those wafers were randomly textured by diluted tetramethylammonium hydroxide (TMAH) solution with ALKA-TEX (GP Solar GmbH) as additives [96]. Then, these wafers were cleaned by sequentially dipping them into 99% room-temperature nitric acid (HNO_3), 69.5% 110 °C HNO_3, and then 0.55% hydrofluoric acid (HF) [97]. All thin-film Si layers were deposited via a multi-chamber radio-frequency (RF, 13.56 MHz) or very-high-frequency (VHF, 40.68 MHz) plasma-enhanced chemical vapor deposition (PECVD) cluster tool (Elettrorava S.p.A.). Besides, additional hydrogen plasma treatment (HPT) and VHF (*i*)nc-Si:H treatment (hereafter called as HPTs) were optionally applied on (*i*)a-Si:H layers (i.e. before depositions of doped Si layers). Note, no change in the thickness of (*i*)a-Si:H was detected via spectroscopic ellipsometry (SE) after 6 min of this VHF (*i*)nc-Si:H treatment.

For cells with Molybdenum oxide (MoO_x), various plasma treatments were additionally applied after the HPTs, and MoO_x layers were thermally evaporated (Provac PRO500S) using a stoichiometric MoO_3 powder source. Afterwards, RF magnetron sputtering (Polyteknic AS) was used for depositing TCO layers. For wafers that feature TCO layers deposited at room temperature, they were annealed in air at 180 °C for 5 min. Eventually, solar cells were finished with different metallization approaches, namely, Ag screen-printing, Ag evaporation and/or Cu-electroplating. Solar cells with screen-printed Ag contacts went through a curing step in the air at 170 °C for 40 min. Alternatively, monofacial cells were electroplated at the front side with Cu grids and thermally evaporated at the rear side with 500-nm-thick Ag, whereas bifacial solar cells were electroplated with Cu grids on both sides. To further improve the anti-reflection effect of solar cells, around 100-nm-thick SiO_x or MgF_2 layer was optionally deposited via e-beam evaporation on the front side of the devices for monofacial devices and both sides for bifacial devices. A geometrical factor of 1.7 was used for calculating the deposition durations for the textured surface based on the depositions on flat substrates. Solar cells reported in this work have a designated area of 4 cm^2.

2.2. Thin-film and device characterizations

Spectroscopic ellipsometry (SE) (M-2000DI system, J.A. Woollam Co., Inc.) was utilized for extracting information such as the thickness, optical constants and optical bandgap of thin film layers deposited on either flat glass (Corning Eagle XG) or wafer substrates. Temperature-dependent dark conductivity (σ_d) measurement was conducted to extract the E_a and σ_d of doped Si thin-film layers. For TCO films, the Hall effect measurement system HMS-5000 from ECOPIA CORP was used to extract the conductivity type, resistivity, carrier mobility (μ_e) and carrier density (N_{TCO}) of TCO films. Spectrophotometer setups (PerkinElmer Lambda 950 and 1050 systems) were used to obtain the wavelength-dependent transmittance (*T*) and reflectance (*R*) of the testing layer, thus obtaining the absorptance (*A*) of the testing layer.

The photoconductance lifetime tester (Sinton WCT-120) was used for measuring the passivation quality during the development of contact stacks for SHJ solar cells and monitoring the passivation quality along the fabrication of solar cells. The effective minority carrier lifetime (τ_{eff}) values reported in this work were extracted at the minority carrier

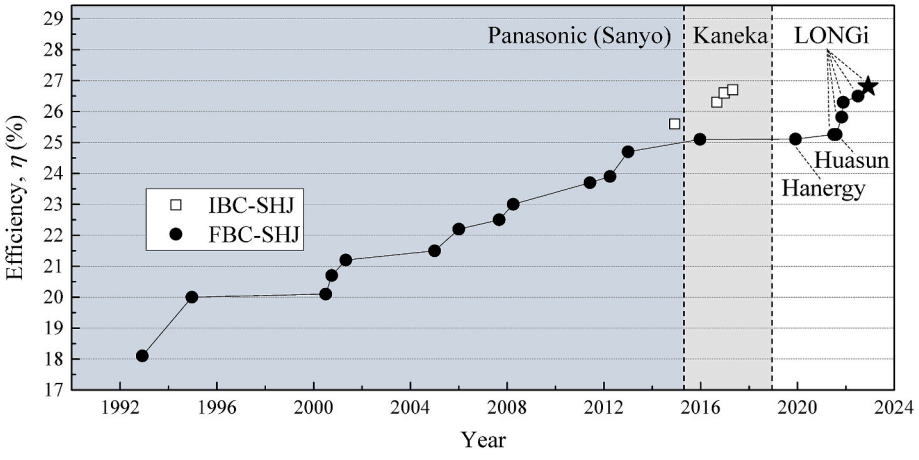

Fig. 2. The certified record efficiency progression of low-thermal budget SHJ solar cells since the first 'HIT' solar cell was reported by Panasonic (Sanyo) [18,34,35,60,71–73,76,81–84,92–95]. Note, the 'HIT' solar cell reported in 1992 was not certified. The star symbol represents the 26.81% FBC-SHJ solar cell. Both LONGi and Huasun achieved a certified efficiency of 25.26% in June and July of 2021, respectively, while LONGi's cell having an area of 244.53 cm^2 and Huasun's cell having an area of 274.5 cm^2, respectively.

density equals to 10^{15} cm^{-3}. The dark current-voltage setup (Cascade Summit probe station CAS33 Microtech) was utilized for characterizing the contact resistivity (ρ_c) of the contact stacks implemented in solar cells. The solar simulator (AAA class Wacom WXS-90S-L2) was used to characterize the illuminated current-voltage performance of fabricated solar cells. Sinton Suns-V_{OC}-150 Illumination-Voltage Tester was employed to assist in the extraction of the series resistance of the device (R_s). An in-house-built external quantum efficiency (EQE) setup with a Fraunhofer ISE-calibrated photodiode was used for evaluating the spectral response of fabricated solar cells. The independently certified *I–V* parameters were obtained from the CalTeC of the Institute for Solar Energy Research Hamelin (ISFH) or Fraunhofer ISE CalLab PV Cells.

2.3. Numerical simulations

Technology computer-aided design (TCAD) Sentaurus from Synopsys Inc. was utilized for device simulations [98]. The optical simulation model Genpro4 was used for optimizing the device design from the light management perspective [99]. First-principle density-functional theory (DFT) calculations were performed for investigating MoO_x and TCO films using Vienna Ab initio Simulation Package (VASP) with projector augmented wave (PAW) method [100,101].

3. Results and discussion

3.1. Selective transport of charge carriers: the transport mechanism

In SHJ solar cells, the collection of charge carriers entails their transport across heterointerfaces or energy barriers. The effectiveness of this process poses strong indications to the eventual performance of solar cells. Therefore, a comprehensive understanding of the underlying physical mechanisms behind the selective transport of charge carriers is crucial for guiding the experimental development of high-efficiency SHJ solar cells. Our TCAD simulations [102,103] suggest the indispensable role of tuning the electrical properties of doped layers and TCO layers for achieving efficient selective transport of charge carriers from c-Si bulk to the TCO. Fig. 3 illustrates a schematic energy band diagram of a typical SHJ solar cell and the corresponding transport mechanisms of charge carriers.

As depicted in Fig. 3, the band bending formed inside c-Si near the c-Si/(*i*)a-Si:H interface is determined by the properties of the (*n*)-type contact stack (c-Si/*i*/*n*/TCO/metal) or (*p*)-type contact stack (c-Si/*i*/*p*/TCO/metal), which is affected by the relative Fermi level position in each compositional material. Besides, due to different bandgaps of c-Si (~1.12 eV) and the (*i*)a-Si:H layer (~1.7 eV), band offsets (ΔE_C for conduction band, ΔE_V for valence band) are formed at the c-Si/(*i*)a-Si:H interface. Typically, ΔE_C (~0.22–0.31 eV) is smaller than the ΔE_V (~0.39–0.61 eV), and the latter is more sensitive to increase with a higher hydrogen content of the (*i*)a-Si:H film [77,104]. Thanks to the band bending and the band offsets, there are highly asymmetric concentrations of electrons and holes within c-Si near each c-Si/(*i*)a-Si:H interface. The large difference in carrier population at c-Si interface suggests a high-quality selective contact [102,105,106]. Subsequently, the accumulated electrons/holes near the c-Si/(*i*)a-Si:H interface can cross the potential barrier formed by the (*i*)a-Si:H/(*n*)-layer or (*i*)a-Si:H/(*p*)-layer via thermionic emission (TE) or with the support of tunneling processes such as direct tunneling (DT) and trap-assisted-tunneling (TAT). The significance of the specific mechanisms varies for the transport of electrons and holes [103,107].

Further, the negative charge collection is based on the transport of electrons towards the conduction band energy. The band bending and the band offset between adjacent materials are mainly defined by the work functions (WF) and electronic properties of the (*n*)-layer and TCO. Electrons cross the potential barriers formed at hetero-interfaces, via TE, DE and TAT processes. As suggested by our simulation study, a (*n*)-layer with a low activation energy (E_a) can enhance the band bending near the c-Si/(*i*)a-Si:H interface, and enable a reduced transport barrier from the (*n*)-layer to the TCO [102]. Besides, a low WF TCO is preferred due to the favourable reduced WF mismatch between the TCO and the (*n*)-layer [102,103,108,109].

The collection of positive charge is based on holes transport up to the (*p*)-layer and electrons in the adjacent TCO layer. Note that at (*p*)-layer/TCO interface charge exchange occurs via band-to-band (B2BT) or TAT tunneling processes [103]. The energy alignment between the valence band of the (*p*)-layer and the conduction band of TCO is essential to discriminate if B2BT or TAT mechanism dominates the charge transfer. In the presence of the aforementioned energy alignment, the transport is based on B2BT in direct energy transition between electrons from the TCO conduction band *jumping* into (*p*)-layer valence band energy state, and vice versa. In the absence of such energy alignment, the charge exchange is based on TAT mechanisms as indirect energy transitions or recombination of electrons from TCO with holes from c-Si at defect

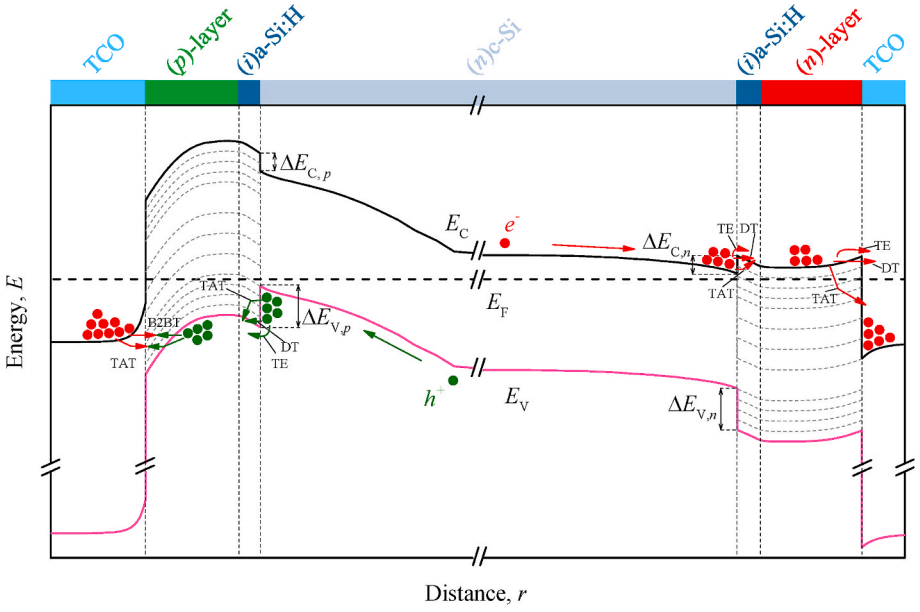

Fig. 3. The schematic energy band diagram of a typical SHJ solar cell with an *n*-type c-Si wafer under dark and thermal equilibrium (the solid black line is the bottom of the conduction band; the solid pink line is the top of the valence band). The ΔE_C and ΔE_V represent the conduction and valence band offsets, respectively. The colored arrows in green and red are for the transport of holes and electrons, respectively. The corresponding transport mechanisms of charger carriers are thermionic emission (TE), direct tunneling (DT), trap-assisted-tunneling (TAT) and band-to-band tunnelling (B2BT). The dashed lines indicate energy levels of different defect states within the bandgap. Those dashed lines also illustrate that the energy band bending can affect the energy levels of defect states. Figure adapted from Ref. [103].

states inside the (*p*)-layer occur near the (*p*)-layer/TCO interface. In general, B2BT is preferred because it implies only direct energy transitions [103,110]. The proper energy alignment can be achieved by adjusting the E_a of (*p*)-layer and/or the WF of TCO. In particular, (*p*)-layer with a low E_a enables more flexibility in TCO electronic properties. Despite a low E_a required, the band bending near the c-Si/(*i*) a-Si:H interface can be also enhanced with a (*p*)-layer that exhibits a high E_g [102].

The transport of charge across heterointerfaces is typically evaluated by the contact resistivity (ρ_c) [103]. It has been proven experimentally that the minimization of ρ_c of SHJ contact stacks is essential for achieving high-efficiency SHJ solar cells [47,111,112]. To understand the physical material parameters affecting ρ_c, we constructed a detailed TCAD simulation framework replicating the transfer length method (TLM) to assess the ρ_c of contact stacks in interest [113,114]. We thus correlate ρ_c to the V_{OC} and *FF* of solar cells [103]. As discussed before, the transport of charge carriers is ultimately driven by material properties that define the Fermi-level energy of layers forming the contact stacks. Therefore, we present in Fig. 4 (for (*p*)-type contact stack) the guidelines for improving the performance of SHJ solar cells with two practically accessible material properties, namely, E_a of doped layers and carrier concentration (N_{TCO}) of TCO. As seen in Fig. 4, different combinations of these two parameters lead to various ρ_c values, which provide insight into distinct dominating transport mechanisms of charge carriers. More details on correlating various transport mechanisms (e.g., B2BT, TAT) and various combinations of E_a and N_{TCO} for both (*n*)- and (*p*)-type contact stacks can be found in our previous work [103]. It is worth noting our simulations were also validated with experimentally fabricated contact stacks that feature various combinations of E_a and N_{TCO} [115].

Overall, as known from our simulations, the V_{OC} of solar cells is solely determined by the quality of the band bending inside the c-Si near its interface with (*i*)a-Si:H, whereas the *FF* is additionally influenced by the quality of the charge carrier transport at the doped-layer/TCO interface. Moreover, reducing the E_a while increasing the N_{TCO} leads to a reduction of ρ_c of contact stacks. Last but not least, the optimization of (*p*)-type contact stack requires greater effort as it is more sensitive to layer properties as compared to (*n*)-type contact stack.

3.2. High-quality (*i*)a-Si:H passivating layer

To realize the high V_{OC} and *FF* of SHJ solar cells, surface recombination must be suppressed by depositing a few nanometers thick optimized hydrogenated intrinsic amorphous silicon ((*i*)a-Si:H) passivating layers on both sides of the c-Si wafer. Typically, the development of (*i*)a-Si:H layer is mainly based on assessing the τ_{eff} and implied V_{OC} of test samples. To enhance the passivation quality of c-Si interfaces by using at thin (*i*)a-Si:H layer, various processing techniques such as tuning the PECVD deposition parameters (e.g., pressure, power, hydrogen dilution, substrate temperature) of (*i*)a-Si:H monolayer [116–120], stacking two or multiple intrinsic layers [93,121–127], applying hydrogen plasma treatment (HPT) [128–134] and performing post-annealing were explored [135–138]. The purpose of this research is twofold: i) to prevent possible detrimental epitaxial growth on the c-Si interface and ii) to ensure passivation support provided by hydrogen atoms inside the layer [136]. We present in Fig. 5(a) the τ_{eff} of symmetrical samples incorporating the bilayer and HPTs passivation approaches. Note that in Fig. 5 (a), 9-nm-thick (*i*)a-Si:H monolayer (or *i*-2) was deposited with a highly hydrogen-diluted plasma. Our bilayer approach combines firstly a 1-nm-thick (*i*)a-Si:H deposited without additional hydrogen dilution (or *i*-1) and then stacking on top 7 or 8-nm-thick *i*-2 layer for subsequential deposition of (*n*)-layer or (*p*)-layer stack, respectively [118]. The HPTs that consist of a hydrogen plasma treatment and a VHF (*i*)nc-Si:H treatment were applied after the deposition of the (*i*)a-Si:H bilayer [131].

As depicted in Fig. 5(a), the (*i*)a-Si:H monolayer delivers a τ_{eff} of 4.3 ms, which can be slightly improved to 4.8 ms when the bilayer is applied. While a notable enhancement of τ_{eff} to 11.2 ms was observed when the bilayer is treated with HPTs. As suggested by our Fourier-transform infrared (FTIR) spectroscopy measurements that characterize the evolution of Si–H bonding configurations and microstructural properties of (*i*)a-Si:H layers, the additional HPTs led to a less-dense and more-hydrogenated (*i*)a-Si:H layer due to the increased formation of large volume deficiencies in the film [118]. In other words, the resulting film containing higher concentrations of polyhydrides can be advantageous for contributing to the passivation of c-Si surface dangling bonds by serving as hydrogen reservoirs during processes with elevated temperatures [139]. Subsequential deposition of (*n*)-layer stack on the HPTs treated bilayer showed further boosted τ_{eff} to 22.3 ms thanks to improved field-effect passivation and enhanced chemical passivation. Particularly, the latter can be attributed to the beneficial hydrogen incorporation during the deposition of (*n*)nc-Si:H, which was deposited with highly hydrogen-diluted plasma conditions [140–142]. However, only 4.6 ms was obtained after deposition of the (*p*)-layer stack. This could be attributed to defect formation in (*i*)a-Si:H layer as a result of Fermi level shift due to the overlaying (*p*)-layer stack [143–146], excessive annealing of the initially deposited *i*/*p* stack during the deposition of the second *i*/*p* stack [143,144], and/or indicates the necessity of further optimization of the deposition conditions of the (*p*)-layer stack. It is worth noting that a more careful choice of *i*-1 and *i*-2 based on their microstructure to form the bilayer, and even with an additional (*i*)a-SiO_x:H or wet-chemical oxidic buffer layer before the deposition of the bilayer, are expected to further benefit the passivation quality [34,93,127].

Although superior passivation quality is essential for realizing high-efficiency SHJ solar cells, the bulk quality of (*i*)a-Si:H layer is also crucial in influencing the charge carrier collection from the c-Si bulk to the TCO, thus affecting the *FF* of solar cells [127,147,148]. We present in Fig. 5

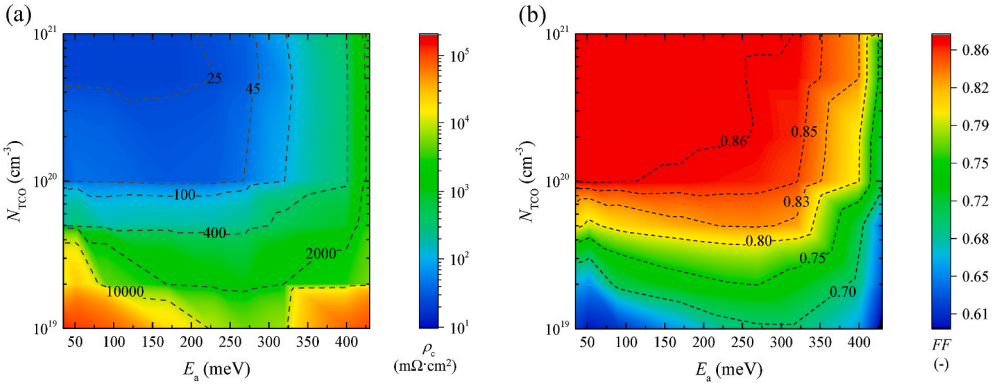

Fig. 4. Contour plot of (a) ρ_c and (b) *FF* of IBC-SHJ solar cell as function of E_a and N_{TCO} at (*p*)-type contact stack. Figure adapted from Ref. [103].

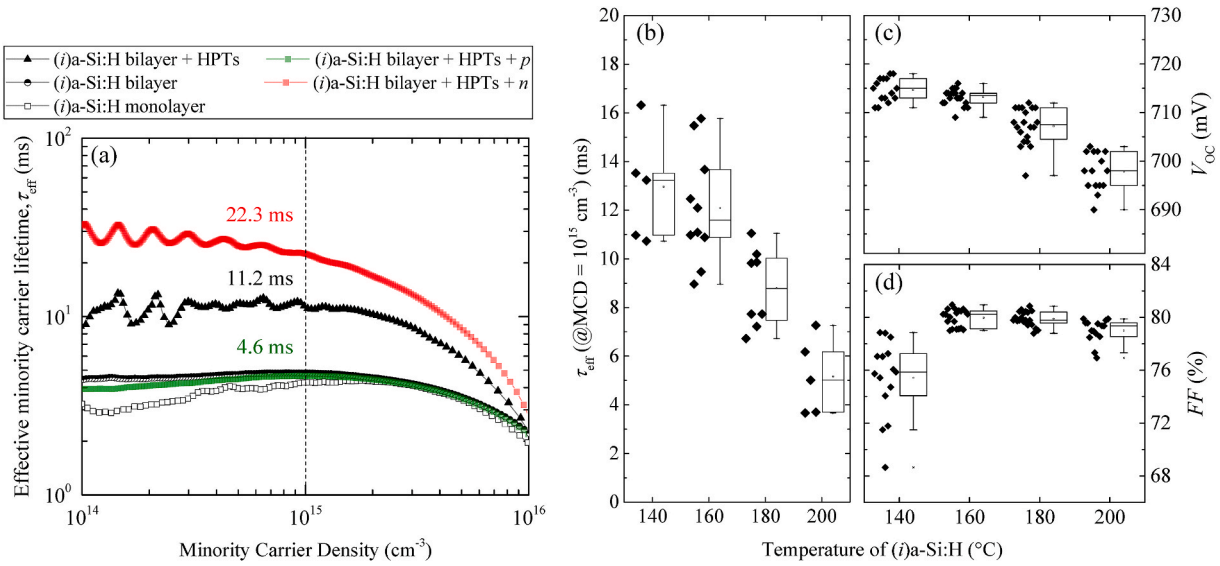

Fig. 5. The effective minority carrier lifetime (τ_{eff}) of (a) symmetrical samples as a function of minority carrier density (MCD), (b) the τ_{eff} of solar cells before metallization and the (c) V_{OC} and (d) *FF* of completed solar cells as a function of deposition temperature of (*i*)a-Si:H underneath both doped layers. In Figure (a), HPTs stand for hydrogen plasma treatments, the *n* represents 3 nm (*n*)nc-Si:H + 2 nm (*n*)a-Si:H, whereas the *p* denotes 5 nm (*p*)nc-SiO$_x$:H + 30 nm (*p*)nc-Si:H. Note in (a), only (*i*)a-Si:H layers were deposited at a substrate temperature of 160 °C while all other layers and HPTs were conducted at a substrate temperature of 180 °C. In (b), the same (*n*)-layer stack is used as that in (a), the (*p*)-layer stack is 5 nm (*p*)nc-SiO$_x$:H + 16 nm (*p*)nc-Si:H. Figure adapted from Ref. [118].

(b)–(d) the effects of (*i*)a-Si:H deposition temperature underneath both doped layers on the passivation quality of solar cell precursors before TCO sputtering, and the illuminated *J-V* performance, especially, the V_{OC} and *FF* of completed solar cells [118]. It should be noted that the (*i*)a-Si:H in Fig. 5(b)–(d) refers to 'bilayer + HPTs' as illustrated in Fig. 5(a). As seen in Fig. 5(b), cell precursors (before TCO sputtering) that feature (*i*)a-Si:H layers deposited at the temperature of 140 °C deliver the highest average τ_{eff}, and consequently, the highest average V_{OC} in completed solar cells (see Fig. 5(c)). However, those cells exhibit deteriorated *FF*s as compared to higher temperature counterparts (see Fig. 5(d)). This observation is comprehended by the FTIR-characterized underdense and hydrogen-rich film obtained with a lower deposition temperature [118]. On the one hand, the (*i*)a-Si:H deposited at a low temperature (140 °C) can relatively enhance hydrogen accumulation [139], promote easier H-diffusion [149,150], prevent possible epitaxial growth caused by *i*-2 [121] and mitigate potential defect formation induced by HPTs [121,151], thus benefitting the V_{OC} of the solar cells. On the other hand, the underdense or porous (*i*)a-Si:H bulk can increase series resistance and contact resistivity in the device [121,148], therefore lowering the *FF*s of solar cells.

In summary, we have optimized the (*i*)a-Si:H passivating layers based on a multi-layer approach together with the additional HPTs. Our research identifies two crucial requirements for optimizing (*i*)a-Si:H layers in high-efficiency SHJ solar cells: (i) achieving excellent surface passivation to minimize losses induced by surface recombinations, and in the meanwhile (ii) ensuring high bulk quality for uninterrupted charge carrier collection.

3.3. Hydrogenated nanocrystalline silicon (nc-Si:H)-based doped layer (stack) for SHJ solar cells

The requirement of a low E_a for doped layers points to implementing materials such as hydrogenated nanocrystalline silicon-based (e.g., nc-Si:H and nc-SiO$_x$:H) layers (E_a lower than 50 meV) other than typically used a-Si:H (E_a of around 200–300 meV) [34,131,140,142,152–166]. The nc-Si:H-based materials contain tiny crystalline grains embedded in the amorphous matrix, and might possess a certain volume fraction of voids [167–169]. Thanks to the more efficient doping in their embedded nanocrystals [170], nc-Si:H-based layers can achieve lower E_a values as compared to that of a-Si:H. Notwithstanding the advantageous electrical properties of nc-Si:H-based layers, their implementation into SHJ solar cells is challenging. This is due to the growth of nc-Si:H, especially, the evolution of their compositions (nanocrystals and amorphous phase) depends on the nature of the substrate and the thickness of the layer [167,171,172]. Those substrate- and thickness-dependent growth characteristics are critically relevant for SHJ solar cells, which feature (*i*)a-Si:H passivating layers and might require limited thicknesses of nc-Si:H-based layers for the optimum device performance. Therefore, efforts have been devoted to facilitating fast nucleation of nanocrystals (minimizing the amorphous incubation phase), which enables efficient band bending near the c-Si surface [34,111,131,140,141,163,173–176]. Accordingly, we developed doped nc-Si:H-based layers with low E_a values (below 50 meV) and (*p*)nc-SiO$_x$:H layers with high E_g values (>2.3 eV in E_{04}) by tuning the PECVD deposition parameters, and implemented them into SHJ solar cells [131].

For electron collection using a single (*n*)nc-SiO$_x$:H layer, we experimentally assessed a minimum thickness of approximately 8 nm is essential to maintain the passivation quality and be effective for electron transport, while the minimum thickness required for (*n*)nc-Si:H and (*n*)a-Si:H can be as thin as 3–4 nm [142,156,177]. This difference is mostly related to their dissimilar capability to incorporate active doping in such thin thicknesses (<10 nm), where (*n*)a-Si:H results to be the most conductive, then followed by (*n*)nc-Si:H and lastly (*n*)nc-SiO$_x$:H. The less conductive (*n*)nc-Si:H-based layers can be linked to their low doping gas (phosphine) flow and highly hydrogen-diluted deposition conditions. The former can lead to lower phosphorous content in the film, while the latter can result in hydrogen-induced dopant inactivation, and alter the amorphous incubation phase of nc-Si:H-based layers to have a microstructure that differs from standard (*n*)a-Si:H [178–180]. Nevertheless, for a 3-nm-thick (*n*)nc-Si:H-based layer that features an E_a value of at least around 600 meV, and yet, it delivers *FF* above 78.6% in solar cells when combined with our aforementioned optimized HPTs (see Fig. 6(a)). The optimized HPTs lead to a H-rich and underdense (*i*)a-Si:H, which provide hydrogen atoms to significantly suppress the surface recombination and may enhance the nucleation of those nc-Si:H-based layers, thus contributing to more efficient selective transport of electrons as can be seen in Fig. 6(a) [103,181–183]. Moreover, the

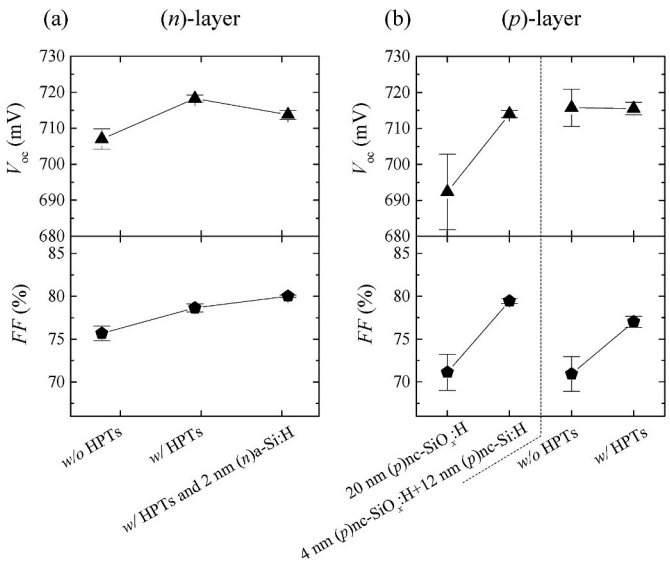

Fig. 6. The effects of HPTs and capping layer on the V_{OC} and *FF* of FBC-SHJ solar cells. In (a), the (*n*)-layer refers to 3-nm-thick (*n*)nc-Si:H. In (b), HPTs were applied for comparing the single (*p*)-layer (20 nm (*p*)nc-SiO_x:H) and bilayer (*p*)-layer stack (4 nm (*p*)nc-SiO_x:H + 12 nm (*p*)nc-SiO_x:H). The influence of HPTs was investigated with solar cells featuring a 4 nm (*p*)nc-SiO_x:H + 16 nm (*p*)nc-Si:H layer stack. Figure adapted from Refs. [142,185].

nucleation could be also promoted thanks to a larger H coverage on the growing surface that increases the surface mobility of SiH_x radicals [184]. It is worth noting that despite the limited active doping in such a thin (*n*)nc-Si:H layer, electrons are capable of tunneling directly from the c-Si to the TCO, making the electron transport to be less dependent on the condition of (*n*)-layer/TCO interface after processing. As a result, as long as the passivation quality is well-maintained, efficient electron collection can still be achieved. A thicker (*n*)nc-Si:H-based layer with well-developed nanocrystals can also result in similar electron transport [103]; however, the device performance can be then limited by its higher parasitic absorption. The above results and discussions suggest the use of a combination of thin (*n*)-layers that ensure a low E_a with a limited thickness. Therefore, we propose the use of 3 nm (*n*)nc-Si:H and 2 nm (*n*)a-Si:H as (*n*)-layer stack to enhance the *FF* of solar cells (see Fig. 6(a)). The additional thin (*n*)a-Si:H can (i) lower the E_a of the (*n*)-contact, (ii) preserve the passivation quality after TCO sputtering, and (iii) prevent surface oxidation of (*n*)nc-Si:H induced by the TCO sputtering [142].

As for hole collection, we combined the optimized (*p*)nc-SiO_x:H and (*p*)nc-Si:H as (*p*)-layer stack for SHJ solar cells. This bilayer stack improves the hole accumulation at the c-Si/(*i*)a-Si:H interface thanks to the high E_g of (*p*)nc-SiO_x:H and the low E_a of (*p*)nc-Si:H, and the latter also promotes the charge carrier exchange at the (*p*)-layer stack/TCO interface. For instance, for cells with only 20-nm-thick (*p*)nc-SiO_x:H as the (*p*)-layer, a high average device series resistance (R_S) of 2310 mΩ·cm^2 and limited *FF*s of around 71.5% were obtained. The addition of a (*p*)nc-Si:H significantly lowered the R_S to approximately 950 mΩ·cm^2 and boosted the *FF* to 79.5% when combining a 4 nm (*p*)nc-SiO_x:H with a 12 nm (*p*)nc-Si:H (see Fig. 6(b)). In the meanwhile, the V_{OC} was also improved from 692 mV to 714 mV by using the optimized (*p*)-layer stack as shown in Fig. 6(b). Those results highlight the critical roles of using the layer with a low E_a for contacting the TCO and additionally enhancing the band bending at the c-Si/(*i*)a-Si:H interface. Besides, by increasing the thickness of the (*p*)nc-Si:H layer, we generally observed increased V_{OC} and *FF* [185]. This is attributed to the decreased E_a of the (*p*)-layer stack with a thicker (*p*)nc-Si:H. Moreover, the optimized HPTs can significantly decrease the R_S of the (*p*)-contact stack from 2920 mΩ·cm^2 to 1440 mΩ·cm^2, thus contributing an increment in *FF* from 70.9% to 77% for solar cells with 4 nm (*p*)nc-SiO_x:H and 16 nm (*p*)nc-Si:H (see Fig. 6(b)).

3.4. Dopant-free molybdenum oxide (MoO_x) as efficient hole collectors

Alternative to Si-based (*p*)-layers that can induce significant parasitic absorption when placed on the illumination side [186], highly transparent Molybdenum oxide (MoO_x) (E_g = 3 eV) was proven to be a promising replacement for efficient hole collection [42,43,47,187]. MoO_x is an (*n*)-type material with a high WF that mismatches with that of the c-Si. As a consequence, band bending near the c-Si interface can be formed and it is in favor of accumulating holes while repelling electrons [188]. Both DFT and TCAD simulations from our group have suggested the importance of a high WF of MoO_x for achieving efficient solar cells [54,189]. While, as shown in Fig. 7(a), our DFT simulation indicates the formation of a strong dipole at the (*i*)a-Si:H/MoO_x interface. This dipole induces a WF attenuation of MoO_x and the degree of attenuation increases with a thicker MoO_x, thus weakening the band bending. Besides, as illustrated in Fig. 7(b), the WF of MoO_x can vary with its stoichiometry, or, the oxidation state of Mo [54]. Especially in practice, the WF of MoO_x is often degraded due to oxygen migration from MoO_x that reacts with adjacent materials. This aspect was also emulated with WF profiles shown in Fig. 7(c) for different (*i*)a-Si:H/MoO_x interfaces, where a thinner MoO_x is needed for saturating the WF when deposited on a less-reactive interface. Therefore, we have developed a plasma treatment technique that is capable to preserve the high WF of MoO_x as verified by XPS measurements [54,189]. Furthermore, through both the TCAD simulations (see Fig. 7(d)) and experimental solar cell results, a MoO_x layer as thin as ~1.7 nm can deliver the optimal trade-off between the WF and WF attenuation, which depends on the thickness of the MoO_x. Following the theoretical findings, we demonstrated a record efficiency of 23.83% for a monofacial SHJ solar cell with this ultra-thin MoO_x as an efficient hole collector [54]. This cell also delivers an active area $J_{SC,EQE}$ of 41.63 mA/cm^2, showcasing the optical advantageous employment of MoO_x for FBC-SHJ solar cells.

3.5. High-mobility TCOs

Despite knowing the significance of the TCO properties in relation to the transport of charge carriers (introduced in Section 3.1), typically, an ideal TCO layer for high-efficiency SHJ solar cells should feature (i) a low sheet resistance (R_{sh}) for allowing efficient lateral transport of charge carriers to the metal electrodes while maintaining broadband transparency in the wavelength range of interest (300–1200 nm), (ii) low contact resistance with the surrounding layers, (iii) suitable refractive index for maximizing the light in-couping into solar cells and (iv) a minimum N_{TCO} of around 10^{20} cm^{-3} for enabling efficient charge carrier transport (see Fig. 4). Note that an increased N_{TCO} can lead to enhanced parasitic free carrier absorption (FCA) for near-infrared light (wavelength above 700 nm) as a result of intra-band transitions within the conduction band [190–192]. To achieve a low R_{sh}, both the μ_e and the N_{TCO} of the TCO can be increased. Therefore, we performed comprehensive studies on developing and implementing various TCOs, especially high-mobility tungsten- and fluorine-doped indium oxides (IWO and IFO), for high-efficiency SHJ solar cells. The material properties of different TCOs and their influence on solar cell performance were explored both experimentally and theoretically (via DFT modellings) [193–195]. With DFT simulations, we were able to calculate the equilibrium geometric, electronic structure, effective electron mass and WF of ITO, IFO, and IWO [195,196]. Especially, the last (simulated WF) provides additional insights for interpreting the effect of different TCO layers on the contact resistivity of doped contact stacks [195].

With optimized deposition conditions, a remarkably high μ_e of 87 cm^{2}V^{-1}s^{-1} was achieved together with an N_{TCO} of 1.2 × 10^{20} cm^{-3} of an optimized IFO:H film. The resulting solar cell exhibited an enhanced $J_{SC,EQE}$ of 1.53 mA/cm^2 (integrated from external quantum efficiency

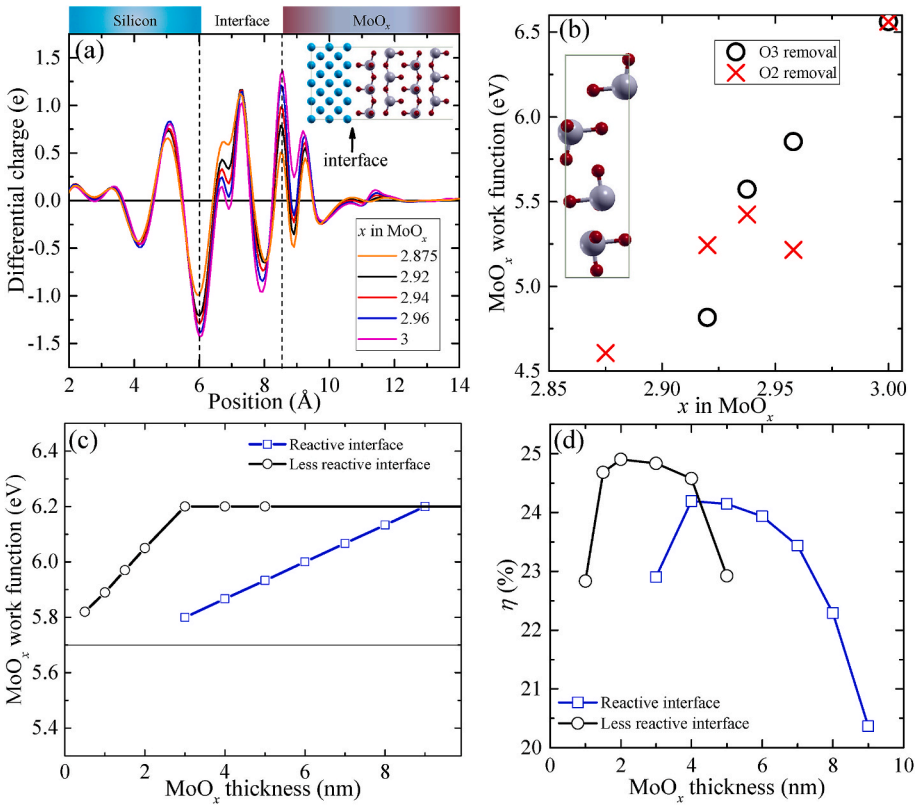

Fig. 7. (a) The differential charge at the Si/MoO_x interface for MoO_x featuring different stoichiometry. The inset illustrates the cross-sectional view of the Si/MoO_x interface, with the dipole forming within the 2.5 Å-thick interface indicated by the arrow. The light blue atoms represent Si, while the grey and the red atoms denote the Mo and O in the MoO_x, respectively. (b) The simulated work functions of MoO_x as a function of the *x* for different oxygen deficiencies: O3 and O2 removal. The unit cell of MoO_3 as modelled in DFT simulations is depicted in the inset. (c) Different work function profiles utilized for simulating a reactive (blue squares) and a less-reactive (*i*)a-Si:H/MoO_x interface (black circles). (d) The simulated conversion efficiency of SHJ solar cells with MoO_x as the hole collector using work function profiles taken from (c). Figure adapted from Ref. [54].

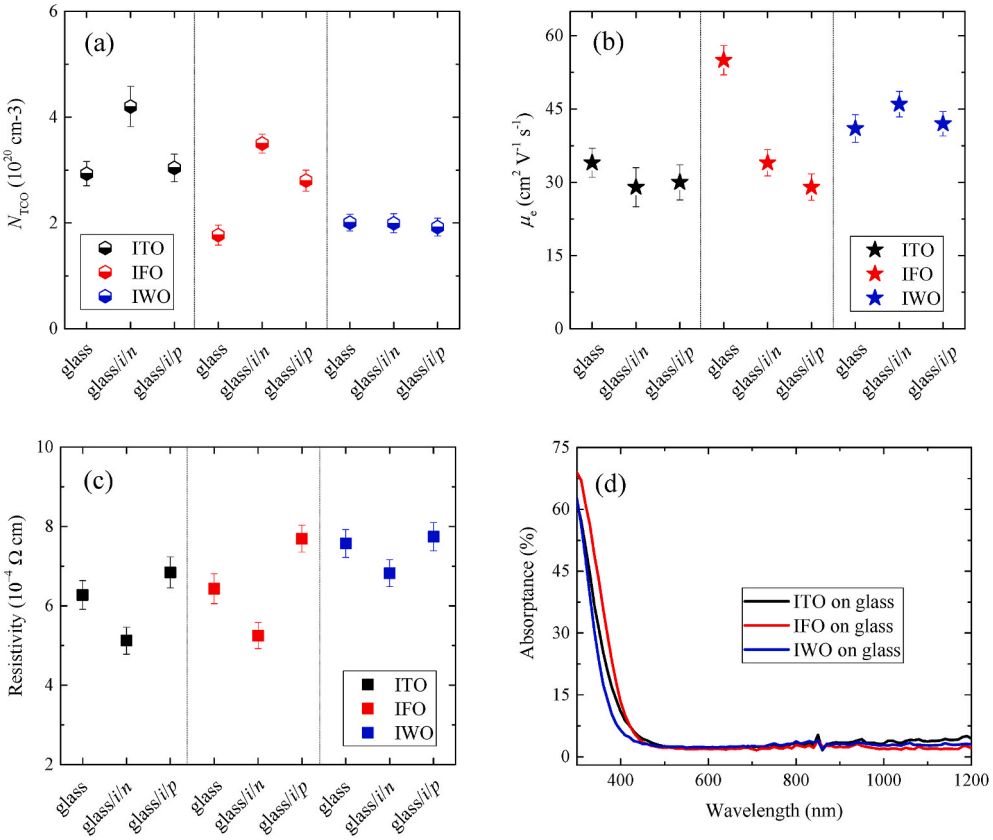

Fig. 8. The (a) carrier density (N_{TCO}), (b) electron mobility (μ_e), (c) resistivity of 75-nm-thick TCO layers deposited on various substrates, and (d) the absorptance of the TCO layers deposited on glass substrates. In (a)–(c), *i*/*n* refers to (*i*)a-Si:H/(*n*)nc-Si:H/(*n*)a-Si:H layer stack and *i*/*p* refers to (*i*)a-Si:H/(*p*)nc-SiO_x:H/(*p*)nc-Si:H layer stack. Figure adapted from Ref. [195].

measurement), compared to our lab-standard ITO counterparts, while maintaining the *FF* [194]. Furthermore, optimized room-temperature sputtered IWO films featuring μ_e of around 45 $cm^2V^{-1}s^{-1}$ and N_{TCO} of approximately 2×10^{20} cm^{-3} were implemented into SHJ solar cells, which also delivered higher $J_{SC,EQE}$ and slightly improved *FF* as compared to cells with our lab-standard ITO [193]. We present in Fig. 8 the opto-electrical properties of various TCO layers deposited on different substrates. As shown in Fig. 8(a)–(c), it is worth noting that we observed substrate-dependent opto-electrical properties of TCO layers. Besides, those properties could be also affected by performing post-annealing on TCO layers. Those changes in TCO properties can be related to effused hydrogen originating from underlying thin-film Si layers, defect passivation by hydrogen, oxygen incorporation and increased crystallization during post-annealing treatment [193,195,197,198]. Therefore, it is necessary to consider the substrate- and process-dependent opto-electrical properties of TCO layers when evaluating the performance of solar cells and performing simulations with properly extracted material properties [195,197]. As depicted in Fig. 8 (d), the reduced absorptance of the IFO and IWO films in the near-infrared wavelength range can be ascribed to their lower N_{TCO} values as indicated in Fig. 8(a). This observation is in accordance with the classical Drude Theory [191]. The absorptance difference in the short-wavelength range reflects the various optical bandgaps of those TCO layers, which are 3.78 eV, 3.80 eV and 3.86 eV for ITO, IFO and IWO films, respectively, as extracted from Tauc plots [199]. This again demonstrates the optical benefits of IFO and IWO films in comparison to the ITO layer [195].

In summary, with optimized (*n*)- and (*p*)-type contact stacks featuring nc-Si:H-based layers, we can minimize ρ_c down to 33 $m\Omega \cdot cm^2$ and 144 $m\Omega \cdot cm^2$, respectively [185]. A low ρ_c of 177 $m\Omega \cdot cm^2$ was also obtained for the MoO_x-based contact stack [54]. Especially, in the view of reducing scarce material usage, such as indium, we experimentally demonstrated that IWO and ITO as thin as 25 nm deliver promisingly low ρ_c of around 80 $m\Omega \cdot cm^2$ and 114 $m\Omega \cdot cm^2$ when combined with *n*- and *p*-layer, respectively [195]. For cells with such thin TCO layers, both low ρ_c values are essential for enabling c-Si wafer-assisted lateral transport [200].

3.6. Cu-electroplating for monofacial and bifacial solar cells

Ag screen printing (SP) is mostly used for manufacturing SHJ solar cells nowadays. The high Ag consumption imposes challenges for the terawatt (TW) implementation of SHJ technology [91]. Besides, the minimum achievable finger width allowed by screen printing is around 20 μm–30 μm [201], which also caps the attainable efficiency due to relatively high shading losses (metal coverages are around 3.25% in our lab-standard Ag SP process). To decrease shading losses while maintaining a low finger resistivity, metal electrodes with a high aspect ratio are required. Such metal electrodes can also facilitate less front metal coverage and allow metal grids with smaller pitch sizes. To fulfil all aforementioned requirements, we developed and optimized a Cu-electroplating metallization approach which can be applied for monofacial plating and simultaneous bifacial plating [202,203]. The latter is extremely desirable for fabricating bifacial SHJ solar cells that can deliver more power with less metal usage than the monofacial counterparts [204,205].

The schematic sketch of the simultaneous bifacial Cu-electroplating setup is illustrated in Fig. 9 (a), where two groups of standard three-electrode cells were immersed in a $CuSO_4$-based electrolyte. The three-electrode consists of the reference electrodes (RE, Ag/AgCl in this case), the working electrode (WE, wafer sample in this case) and the counter electrodes (CE, Cu sheets in this case). We utilized two independent Metrohm Autolab potentiostat tools for independently controlling the Cu-electroplating on both sides. Specifically, a full area of 100-nm-thick thermally evaporated Ag seed layer was first deposited on top of the TCO layer. Then, photolithography steps including applying photoresist, exposure and development were conducted to cover the area that was not intended to form Cu grids with photoresist. Then, the patterned area with the Ag seed layer exposed was electroplated with Cu. Afterwards, the remaining photoresist and the Ag seed layer underneath were removed. Detailed descriptions of the Cu-plating process are available in our publications [202,203].

With this approach, the usage of Ag is significantly minimized. Moreover, it also enables ultra-fine (width ≤15 μm) and highly conductive Cu fingers with high aspect ratios (see Fig. 9) [202,203]. Typically, the line resistivity is 10.0 ± 5.0 μΩ·cm for our lab-standard Ag SP, while it is only 1.7 ± 0.1 μΩ·cm in the case of Cu-electroplated contacts. In addition, unlike our lab-standard screen-printed Ag grids, the electroplated Cu grids appear to be void-free in the bulk and conformal on the surface [203]. Overall, Cu-plating allows more optimum design of metal grids with smaller pitch sizes (915 μm) than Ag screen printing (around 1300–1900 μm) while only featuring a small metal coverage of 1.55%, which significantly enhanced both the electrical and optical performance of our SHJ solar cells [203].

3.7. Optimum light management

Apart from minimizing the metal shading loss as discussed in section 3.6, parasitic absorption and reflection losses should also be minimized [186]. The parasitic absorption is reduced by applying at the front side our developed (*n*)-type nc-Si-based or MoO_x-based layer stacks, as either of them is more transparent than (*n*)a-Si:H or Si-based (*p*)-layers, respectively, mainly thanks to their higher bandgaps [54,142]. Moreover, the use of high-mobility IFO:H and IWO TCO films can also lower

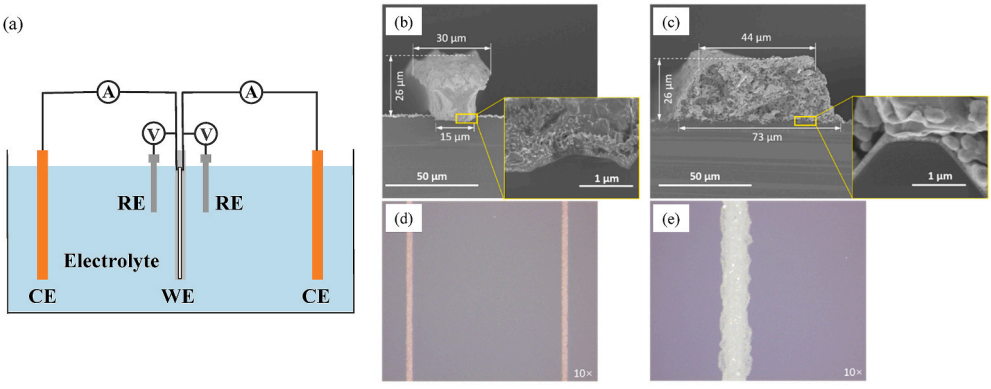

Fig. 9. The (a) schematic sketch of the simultaneous bifacial Cu-electroplating setup, the (b), (c) scanning electron microscope (SEM) and (d), (e) optical microscope images of electroplated Cu fingers, and screen-printed Ag contacts. In (a), WE represents the working electrode (wafer sample), RE stands for the reference electrode (Ag/AgCl) and CE refers to the counter electrode (Cu sheets).

the parasitic absorption as compared to standardly used ITO layers [193, 194]. To suppress the reflection loss, the optical simulation model Genpro4, which integrates ray-tracing and wave-optics, was employed for optimizing the optical design of devices [99]. With spectroscopic ellipsometry, the optical constants and thicknesses of all layers applied in solar cells were experimentally extracted and used as inputs for optical simulations. For instance, a SiO_x or MgF_2 layer with an optimum thickness was added to form a double-layer anti-reflection coating (DLARC) with the adjacent TCO layer [193,206]. The application of optimized DLARC, which allows maximum light coupling into the solar cells, can facilitate the TCO reduction in both monofacial and bifacial SHJ solar cells [195]. In Fig. 10, we present the schematic sketch of the fabricated 24.18%-efficient FBC-SHJ solar cell (see Table 1), its measured EQE and the simulated absorptance spectra with Genpro4. As illustrated in Fig. 10, the overall good correspondence between the measured EQE spectrum and simulated absorptance of the c-Si absorber provides additional insights into the optical constraints of the device, which can guide further improvements in device light management.

3.8. *The evolution of FF and the best monofacial and bifacial FBC-SHJ solar cells*

As a result of the abovementioned design strategies for achieving efficient selective transport and collection of charge carriers for high-efficiency SHJ solar cells, we present in Fig. 11 the followed roadmap of *FF* development for FBC-SHJ solar cells that employ nc-Si:H-based contact stacks in the PVMD group. Initially, due to the limited insights on charge carrier transport and the insufficient control over crucial processing steps and materials, we observed a rather large spread of *FF* for cells with unoptimized nc-Si-based contact stacks. After performing rigorous device simulations, we gained a better comprehension of the transport mechanisms of charge carriers. The simulations also revealed key accessible material parameters that can be utilized to efficiently develop and optimize the contact stacks. Specifically, with different optimization objectives as depicted in Fig. 11, we progressively improved in a few years the maximum achievable *FF* and constrained the distribution of the obtained *FF*s. In this contribution, we present the best attained *FF* value of 83.3%, which can be further enhanced with the continuous process and material optimizations on the passivation, the effectiveness of the contact stack and the metallizations.

Lastly, to evaluate the developed contact stacks with optimized DLARC and Cu-electroplating metallization, monofacial and bifacial FBC-SHJ solar cells were fabricated with the structures shown in Fig. 12. Rear junction solar cells with doped nc-Si:H-based contact stacks are sketched in Fig. 12(a) and (b). Front junction solar cells with MoO_x-based contact stack are illustrated in Fig. 12(c) and (d). External parameters of fabricated best solar cells are presented in Table 1. Monofacial FBC-SHJ solar cells featuring doped nc-Si:H-based contact stacks reached an efficiency of 24.18% with a *FF* of 83.30%, while bifacial solar cells demonstrated efficiency approaching 23% (*n*-side illumination) with room for further optimization. A bifaciality factor of 0.95 is calculated for this bifacial solar cell. Alternatively, front junction SHJ solar cells with MoO_x window layer obtained efficiencies of 23.83% and 23.25% (*p*-side illumination) for monofacial and bifacial configurations, respectively. A high bifaciality factor of 0.98 was obtained for the bifacial cell endowed with MoO_x. All devices feature less TCO usage (11%–56% less) as compared to our lab-standard TCO thicknesses. Especially, bifacial solar cells provide a more effective way to reduce TCO and metal consumption as compared to their monofacial counterparts.

4. 'Beyond' standard FBC-SHJ architectures

The aforementioned results show our lab-scale R&D experience in processing and optimizing low-thermal budget FBC-SHJ solar cells. With a similar approach, the industry reported recently a record conversion efficiency of 26.81% for single-junction c-Si devices using SHJ technology, which achieved almost its maximal potential [34]. This excellent result indicates that SHJ technology is ready to explore alternative device architectures to simplify the process while being highly performant. In this context, we propose here novel solar cell structures and point out their corresponding advantages and potential drawbacks or limitations. To do so, we utilized TCAD simulations tools [98], which were consistently coupled with Genpro4 [99], to simulate different solar cell architectures under one sun illumination accounting for the same c-Si parametrization (i.e. 2 Ω·cm, 100-μm-thick with 2% front metallization) as the optimized reference baseline SHJ solar cell. Fig. 13 shows the schematic sketches of the proposed device configurations with reference stacks of layers. Note that for the sake of simplicity, we report the structure with better light management between front or rear junction (FJ or RJ) schemes considering realistic choices of thin-film layers. As a result, we evaluated architectures featuring dopant-free, TCO-selective and buried junctions with FJ structures, whereas the reference baseline SHJ solar cells and devices with localized contacts were assessed with RJ configurations. Table 2 summarizes the simulated external parameters of the various SHJ-based device structures.

As seen in Table 2, for the reference baseline SHJ device (see Fig. 13 (a)), we simulated an efficiency of 26.82% with a V_{OC} of 0.753 V, a *FF* of 0.869 and a J_{SC} of 40.99 mA/cm^2. Note that we considered (*n*)-layer on the front as such a functional layer is typically less absorptive than a functional (*p*)-layer [131]. Further, SHJ solar cells with dopant-free passivating contacts are a viable alternative to substitute rather parasitically absorptive doped Si-based thin-film layers when placed on the illumination side. With this device configuration as shown in Fig. 13(b), we performed simulations based on our optimized ultra-thin MoO_x layer on the front side [54], which led to an increment in J_{SC} to 41.13

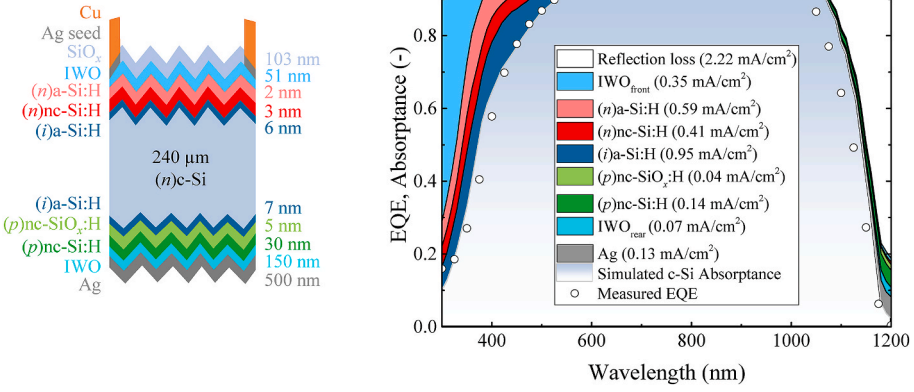

Fig. 10. The schematic sketch of the fabricated 24.18%-efficient SHJ solar cell (left), and its EQE and simulated absorptance spectra (right). The mismatch between the EQE spectrum and the simulated absorptance profiles can be attributed to (i) the non-ideal collection efficiency of charge carriers in EQE measurement while the simulation considers only optical effects, (ii) underestimated absorption of TCO in the near-infrared range due to limited sensitivity of the reflective-type SE used for extracting the extinction coefficient [207], (iii) possible non-negligible plasmonic absorption of rear Ag is not considered in the simulation [208].

Table 1
Best fabricated monofacial and bifacial FBC-SHJ solar cells with Cu-electroplating and thinner TCO.

Cell type	TCO front/rear (nm)	Illumination side	V_{OC} (mV)	J_{SC} (mA/cm^2)	*FF* (%)	η (%)	TCO usage[a]	Bifaciality factor
(a) Monofacial	50/150	Front (*n*-side)	726.0	39.97	83.30	24.18	11% less	–
(b) Bifacial[b]	25/75	Front (*n*-side)	719.5	38.68	82.07	22.84	56% less	0.95
		Rear (*p*-side)	718.4	36.79	81.93	21.65		
(c) Monofacial (MoO_x)[b]	50/150	Front (*p*-side)	721.4	40.20	82.18	23.83	11% less	–
(d) Bifacial (MoO_x)[b]	50/50	Front (*p*-side)	716.2	39.71	81.74	23.25	56% less	0.98
		Rear (*n*-side)	715.6	38.83	81.86	22.75		

[a] Compared to our lab-standard 75 nm front and 150 nm rear TCO thicknesses.
[b] Independently certified at ISFH CalTeC or Fraunhofer ISE CalLab PV Cells.

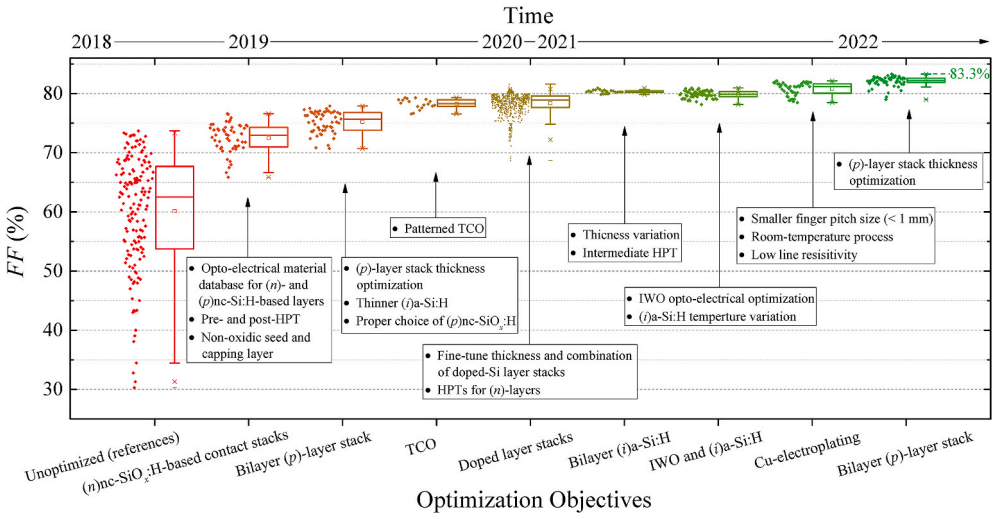

Fig. 11. The followed roadmap of *FF* development for FBC-SHJ solar cells with nc-Si:H-based contact stacks in the PVMD group. The roadmap includes detailed optimization objectives and approximate periods of different development steps. The data points in the plot represent the *FF* of individual solar cells.

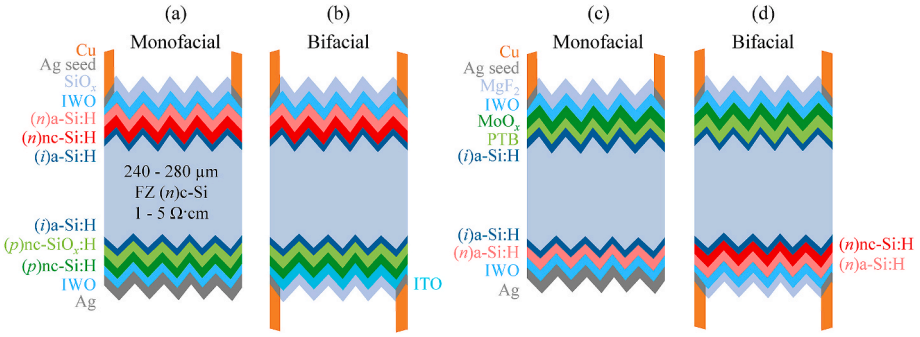

Fig. 12. Monofacial and bifacial FBC-SHJ solar cells with electroplated Cu electrodes with (a), (b) nc-Si:H-based contact stack and (c), (d) MoO_x-based hole contact stack.

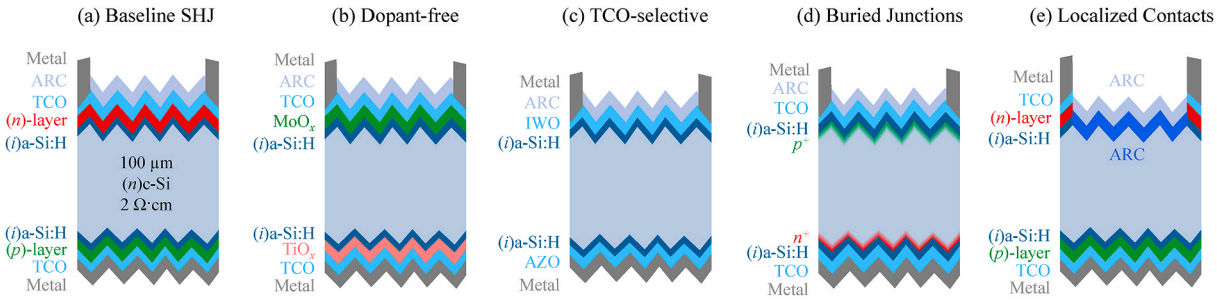

Fig. 13. Schematic sketches of various SHJ-based device architectures with reference stacks of layers, namely, baseline SHJ solar cells, dopant-free SHJ solar cells, TCO-selective SHJ solar cells [209], SHJ solar cells with buried junctions [210] and SHJ solar cells with localized contacts [211].

Table 2
Simulated external parameters of various SHJ-based device architectures.

	J_{SC} (mA/cm^2)	V_{OC} (V)	*FF* (−)	η (%)
Baseline SHJ	40.99	0.753	0.869	26.82
Dopant-free	41.13	0.753	0.870	26.96
TCO-selective	41.19	0.753	0.863	26.76
Buried Junction	41.33	0.741	0.852	26.12
Localized Contacts	42.34	0.753	0.865	27.60

mA/cm^2. As a result, the calculated performance of the dopant-free structure is 0.14%$_{abs}$ higher than the simulated baseline SHJ solar cells.

Moreover, aiming at having more transparent contacts and simpler processes, we propose a solar cell structure in which front and rear TCOs act as HTL or ETL layers, without doped or dopant-free layers (see Fig. 13(c)) [209]. As expected, the external parameters depend on the opto-electrical properties of the TCO, in particular the one acting as the HTL. In this regard, promising TCO candidates are those that can induce an electrical field within the bulk of the c-Si absorber due to their relatively high work function. For instance, IWO is one such candidate [193]. Similarly, Al-doped zinc oxide (AZO) exhibits the properties of being a promising candidate as the ETL [212]. As a result, for TCO-selective devices, we calculated 41.19 mA/cm^2, 0.753 V, 0.863 and 26.76% as J_{SC}, V_{OC}, *FF* and conversion efficiency, respectively. Such parameters are similar to those calculated for the baseline SHJ structure. Nevertheless, the main advantage of such solar cells stands in the fact that fewer layers are used, besides the eventual practical challenges, such as realizing a thin (*i*)a-Si:H layer (stack) being resilient against subsequent TCO processing. Moreover, the use of less damaging TCO deposition techniques, such as pulsed-laser deposition [213] and reactive plasma deposition [214,215], is expected to also contribute to the experimental optimizations of TCO-selective SHJ solar cells.

Taking the TCO-selective structure as a reference but to allow more flexibility in choosing TCO materials, we propose to combine this approach with a c-Si wafer that has surfaces been previously Boron- and/or Phosphorus-diffused (see Fig. 13(d)). The purpose of this doping profile is to enable a built-in internal electrical field inside the bulk fulfilling the junction condition similar to the in-diffusion of cells with poly-Si-based carrier-selective passivating contacts [216–218]. With this structure, we were able to select rather transparent TCOs on both sides that lead to a simulated J_{SC} of 41.33 mA/cm^2, which is 0.2 mA/cm^2 higher than the dopant-free option. Despite the optical gain, we observed a V_{OC} drop of 0.12 V and a *FF* reduction of 1.7%$_{abs}$ as compared to the baseline SHJ solar cells, due to the increased intrinsic recombination in the highly doped regions. Accordingly, the calculated conversion efficiency is 26.12% for SHJ solar cells with buried junctions.

Last but not least, we evaluated a solar cell structure with the same contact stack as our baseline SHJ devices, but the front contact layers, namely, (*i*)a-Si:H, (*n*)-layer and TCO are localized beneath the front metal contact as depicted in Fig. 13(e). With this structure, we obtained a 1.35 mA/cm^2 increase in J_{SC} which results in 0.78%$_{abs}$ efficiency gain with respect to the baseline SHJ solar cells, leading to a conversion efficiency of 27.60%. The experimental development of this solar cell architecture might require the fabrication of proof-of-concept intermediate structures such as cells with localized TCO, or devices with localized TCO and doped layers. It is worth noting, besides all these proposed architectures as shown in Fig. 13 can be adapted to be bifacial, they can be also modified to be used as bottom cells for tandem applications, for example, with perovskite top cells.

5. Conclusions

This work presents an overview of strategies for realizing high-efficiency FBC-SHJ solar cells with the assistance of advanced opto-electrical simulations. Different optimization aspects are briefly discussed, namely, the development of high-quality (*i*)a-Si:H passivating layer, efficient selective transport of charge carriers from c-Si to TCO, optimization of metallizations and light management of the solar cells. Developed nc-Si-based contact stacks are implemented into Cu-electroplated monofacial and bifacial FBC-SHJ solar cells, achieving efficiencies of 24.18% and 22.84%, respectively. Alternative MoO_x-based contact stacks deliver efficiencies of 23.83% and 23.25% for monofacial and bifacial configurations, respectively. As compared to monofacial solar cells, bifacial solar cells provide a more effective way to significantly reduce the usage of In and Ag. Lastly, we propose multiple innovative solar cell designs based on SHJ technology. Their potential performance was evaluated and compared. The FBC-SHJ solar cells that feature localized contacts were simulated to achieve a practical maximal efficiency of 27.60%, which surpasses that of the baseline SHJ solar cells mainly due to the significantly reduced parasitic absorptions.

CRediT authorship contribution statement

Yifeng Zhao: Writing – original draft, Visualization, Validation, Software, Methodology, Investigation, Formal analysis, Data curation, Conceptualization. **Paul Procel:** Writing – original draft, Software, Investigation, Formal analysis, Data curation, Conceptualization. **Can Han:** Writing – review & editing, Validation, Software, Methodology, Investigation, Formal analysis, Data curation, Conceptualization. **Liqi Cao:** Writing – review & editing, Validation, Methodology, Investigation, Formal analysis, Data curation, Conceptualization. **Guangtao Yang:** Writing – review & editing. **Engin Özkol:** Writing – review & editing. **Alba Alcañiz:** Writing – review & editing, Software, Investigation. **Katarina Kovačević:** Writing – review & editing, Investigation. **Gianluca Limodio:** Writing – review & editing, Methodology. **Rudi Santbergen:** Writing – review & editing, Software. **Arno Smets:** Writing – review & editing, Formal analysis. **Arthur Weeber:** Writing – review & editing, Supervision, Funding acquisition. **Miro Zeman:** Writing – review & editing, Supervision, Project administration, Funding acquisition. **Luana Mazzarella:** Writing – review & editing, Validation, Supervision, Methodology, Investigation, Formal analysis, Conceptualization. **Olindo Isabella:** Writing – review & editing, Supervision, Funding acquisition.

Declaration of competing interest

The authors declare that they have no known competing financial interests or personal relationships that could have appeared to influence the work reported in this paper.

Data availability

Data will be made available on request.

Acknowledgement

This study receives financial support from the NWO Joint Solar Program III (680-91-011) and technical support from PVMD group technicians, especially Martijn Tijssen, Stefaan Heirman and Daragh O'Connor. The authors would like to also thank René van Swaaij from the PVMD group for insightful discussions as well as Peyman Taheri from the Mechanical, Maritime and Materials Engineering faculty of the Delft University of Technology for supporting our experimental campaigns. The authors would like to thank Frans D. Tichelaar from the Kavli Institute of Technology of the Delft University of Technology for performing high-resolution transmission electron microscopy measurements and energy-dispersive X-ray elemental mapping analyses.

References

[1] E. Becquerel, La lumière, ses causes et ses effets, Firmin Didot frères, fils et cie, 1867.
[2] Fraunhofer Institute for Solar Energy Systems, Photovoltaics Report, 2022.
[3] K.H. Kim, C.S. Park, J.D. Lee, J.Y. Lim, J.M. Yeon, I.H. Kim, E.J. Lee, Y.H. Cho, Record high efficiency of screen-printed silicon aluminum back surface field solar cell: 20.29%, Jpn. J. Appl. Phys. 56 (2017), 08MB25 https://doi.org/10.7567/JJAP.56.08MB25.
[4] M. Hermle, F. Feldmann, M. Bivour, J.C. Goldschmidt, S.W. Glunz, Passivating contacts and tandem concepts: approaches for the highest silicon-based solar cell efficiencies, Appl. Phys. Rev. 7 (2020), 21305, https://doi.org/10.1063/1.5139202.
[5] A.W. Blakers, A. Wang, A.M. Milne, J. Zhao, M.A. Green, 22.8% efficient silicon solar cell, Appl. Phys. Lett. 55 (1989) 1363–1365, https://doi.org/10.1063/1.101596.
[6] VDMA, International Technology Roadmap for Photovoltaic, thirteenth ed., 2022.
[7] T. Dullweber, J. Schmidt, Industrial silicon solar cells applying the passivated emitter and rear cell (PERC) concept—a review, IEEE J. Photovoltaics 6 (2016) 1366–1381, https://doi.org/10.1109/JPHOTOV.2016.2571627.
[8] D. Kray, M. Hermle, S.W. Glunz, Theory and experiments on the back side reflectance of silicon wafer solar cells, Prog. Photovoltaics Res. Appl. 16 (2008) 1–15, https://doi.org/10.1002/pip.769.
[9] J. Zhao, A. Wang, M.A. Green, 24% efficient PERL structure silicon solar cells, in: IEEE Conf. Photovolt. Spec., IEEE, 1990, pp. 333–335, https://doi.org/10.1109/PVSC.1990.111642.
[10] J. Zhao, A. Wang, M.A. Green, 24.5% Efficiency silicon PERT cells on MCZ substrates and 24.7% efficiency PERL cells on FZ substrates, Prog. Photovoltaics Res. Appl. 7 (1999) 471–474, https://doi.org/10.1002/(SICI)1099-159X(199911/12)7:6%3C471::AID-PIP298%3E3.0.CO;2-7.
[11] M.A. Green, The path to 25% silicon solar cell efficiency: history of silicon cell evolution, Prog. Photovoltaics Res. Appl. 17 (2009) 183–189, https://doi.org/10.1002/pip.892.
[12] M.A. Green, E.D. Dunlop, J. Hohl-Ebinger, M. Yoshita, N. Kopidakis, K. Bothe, D. Hinken, M. Rauer, X. Hao, Solar cell efficiency tables (Version 60), Prog. Photovoltaics Res. Appl. 30 (2022) 687–701, https://doi.org/10.1002/pip.3595.
[13] Trina Solar, 210 PERC Cell Efficiency Achieves 24.5%, Trina Solar Breaks World Record for the 24th Time, 2022. https://www.trinasolar.com/en-glb/resources/newsroom/en210-perc-cell-efficiency-achieves-245-trina-solar-breaks-world-record-24th-time.
[14] A. Richter, S.W. Glunz, F. Werner, J. Schmidt, A. Cuevas, Improved quantitative description of Auger recombination in crystalline silicon, Phys. Rev. B Condens. Matter 86 (2012) 1–14, https://doi.org/10.1103/PhysRevB.86.165202.
[15] S.C. Baker-Finch, K.R. McIntosh, D. Yan, K.C. Fong, T.C. Kho, Near-infrared free carrier absorption in heavily doped silicon, J. Appl. Phys. 116 (2014), 63106, https://doi.org/10.1063/1.4893176.
[16] D. Yan, A. Cuevas, Empirical determination of the energy band gap narrowing in highly doped n+ silicon, J. Appl. Phys. 114 (2013), 44508, https://doi.org/10.1063/1.4816694.
[17] D. Yan, A. Cuevas, Empirical determination of the energy band gap narrowing in p+ silicon heavily doped with boron, J. Appl. Phys. 116 (2014), 194505, https://doi.org/10.1063/1.4902066.
[18] M. Tanaka, M. Taguchi, T. Matsuyama, T. Sawada, S. Tsuda, S. Nakano, H. Hanafusa, Y. Kuwano, Development of new a-Si/c-Si heterojunction solar cells: ACJ-HIT (artificially constructed junction-heterojunction with intrinsic thin-layer), Jpn. J. Appl. Phys. 31 (1992) 3518, https://doi.org/10.1143/JJAP.31.3518.
[19] F. Feldmann, M. Bivour, C. Reichel, M. Hermle, S.W. Glunz, Passivated rear contacts for high-efficiency n-type Si solar cells providing high interface passivation quality and excellent transport characteristics, Sol. Energy Mater. Sol. Cells 120 (2014) 270–274, https://doi.org/10.1016/j.solmat.2013.09.017.
[20] U. Römer, R. Peibst, T. Ohrdes, B. Lim, J. Krügener, E. Bugiel, T. Wietler, R. Brendel, Recombination behavior and contact resistance of n+ and p+ poly-crystalline Si/mono-crystalline Si junctions, Sol. Energy Mater. Sol. Cells 131 (2014) 85–91, https://doi.org/10.1016/j.solmat.2014.06.003.
[21] H. Fujiwara, T. Kaneko, M. Kondo, Application of hydrogenated amorphous silicon oxide layers to c-Si heterojunction solar cells, Appl. Phys. Lett. 91 (2007), 133508, https://doi.org/10.1063/1.2790815.
[22] D. Pysch, M. Bivour, M. Hermle, S.W. Glunz, Amorphous silicon carbide heterojunction solar cells on p-type substrates, Thin Solid Films 519 (2011) 2550–2554, https://doi.org/10.1016/j.tsf.2010.12.028.
[23] G. Nogay, J. Stuckelberger, P. Wyss, Q. Jeangros, C. Allebé, X. Niquille, F. Debrot, M. Despeisse, F.-J. Haug, P. Loper, C. Ballif, Silicon-rich silicon carbide hole-selective rear contacts for crystalline-silicon-based solar cells, ACS Appl. Mater. Interfaces 8 (2016) 35660–35667, https://doi.org/10.1021/acsami.6b12714.
[24] G. Nogay, Full-area Passivating Contacts with High and Low Thermal Budgets: Solutions for High Efficiency C-Si Solar Cells, EPFL, 2018, https://doi.org/10.5075/epfl-thesis-8707.
[25] A. Ingenito, G. Nogay, Q. Jeangros, E. Rucavado, C. Allebé, S. Eswara, N. Valle, T. Wirtz, J. Horzel, T. Koida, M. Morales-Masis, M. Despeisse, F.-J. Haug, P. Löper, C. Ballif, A passivating contact for silicon solar cells formed during a single firing thermal annealing, Nat. Energy 3 (2018) 800–808, https://doi.org/10.1038/s41560-018-0239-4.
[26] M. Boccard, Z.C. Holman, Amorphous silicon carbide passivating layers for crystalline-silicon-based heterojunction solar cells, J. Appl. Phys. 118 (2015), 65704, https://doi.org/10.1063/1.4928203.
[27] M.W.M. van Cleef, F.A. Rubinelli, R. Rizzoli, R. Pinghini, R.E.I. Schropp, W.F. van der Weg, Amorphous silicon carbide/crystalline silicon heterojunction solar cells: a comprehensive study of the photocarrier collection, Jpn. J. Appl. Phys. 37 (1998) 3926, https://doi.org/10.1143/JJAP.37.3926.
[28] J. Stuckelberger, G. Nogay, P. Wyss, Q. Jeangros, C. Allebé, F. Debrot, X. Niquille, M. Ledinsky, A. Fejfar, M. Despeisse, F.-J. Haug, P. Löper, C. Ballif, Passivating electron contact based on highly crystalline nanostructured silicon oxide layers for silicon solar cells, Sol. Energy Mater. Sol. Cells 158 (2016) 2–10, https://doi.org/10.1016/j.solmat.2016.06.040.
[29] G. Yang, P. Guo, P. Procel, A. Weeber, O. Isabella, M. Zeman, Poly-crystalline Silicon-Oxide Films as Carrier-Selective Passivating Contacts for C-Si Solar Cells, 2018, https://doi.org/10.1063/1.5027547.
[30] I. Mack, J. Stuckelberger, P. Wyss, G. Nogay, Q. Jeangros, J. Horzel, C. Allebé, M. Despeisse, F.-J. Haug, A. Ingenito, P. Loper, C. Ballif, Properties of mixed phase silicon-oxide-based passivating contacts for silicon solar cells, Sol. Energy Mater. Sol. Cells 181 (2018) 9–14, https://doi.org/10.1016/j.solmat.2017.12.030.
[31] G. Yang, C. Han, P. Procel, Y. Zhao, M. Singh, L. Mazzarella, M. Zeman, O. Isabella, Oxygen-alloyed poly-Si passivating contacts for high-thermal budget c-Si heterojunction solar cells, Prog. Photovoltaics Res. Appl. (2021), https://doi.org/10.1002/pip.3472.
[32] M. Singh, R. Santbergen, L. Mazzarella, A. Madrampazakis, G. Yang, R. Vismara, Z. Remes, A. Weeber, M. Zeman, O. Isabella, Optical characterization of poly-SiOx and poly-SiCx carrier-selective passivating contacts, Sol. Energy Mater. Sol. Cells 210 (2020), 110507, https://doi.org/10.1016/j.solmat.2020.110507.
[33] A. Ingenito, G. Nogay, J. Stuckelberger, P. Wyss, L. Gnocchi, C. Allebé, J. Horzel, M. Despeisse, F.-J. Haug, P. Löper, C. Ballif, Phosphorous-doped silicon carbide as front-side full-area passivating contact for double-side contacted c-Si solar cells, IEEE J. Photovoltaics 9 (2018) 346–354, https://doi.org/10.1109/JPHOTOV.2018.2886234.
[34] H. Lin, M. Yang, X. Ru, G. Wang, S. Yin, F. Peng, C. Hong, M. Qu, J. Lu, L. Fang, C. Han, P. Procel, O. Isabella, P. Gao, Z. Li, X. Xu, Silicon heterojunction solar cells with up to 26.81% efficiency achieved by electrically optimized nanocrystalline-silicon hole contact layers, Nat. Energy (2023), https://doi.org/10.1038/s41560-023-01255-2.
[35] K. Yoshikawa, H. Kawasaki, W. Yoshida, T. Irie, K. Konishi, K. Nakano, T. Uto, D. Adachi, M. Kanematsu, H. Uzu, K. Yamamoto, Silicon heterojunction solar cell with interdigitated back contacts for a photoconversion efficiency over 26, Nat. Energy 2 (2017), 17032, https://doi.org/10.1038/nenergy.2017.32.
[36] JinkoSolar's JinkoSolar, High-efficiency N-type Monocrystalline Silicon Solar Cell Sets Our New Record with Maximum Conversion Efficiency of 26.4%, 2022. https://www.jinkosolar.com/en/site/newsdetail/1827. (Accessed 23 May 2023).
[37] F. Haase, C. Hollemann, S. Schäfer, A. Merkle, M. Rienäcker, J. Krügener, R. Brendel, R. Peibst, Laser contact openings for local poly-Si-metal contacts enabling 26.1%-efficient POLO-IBC solar cells, Sol. Energy Mater. Sol. Cells 186 (2018) 184–193, https://doi.org/10.1016/j.solmat.2018.06.020.
[38] Akcome, Industrialized Technology of High-Efficiency HJT Product and its Challenges, 5th International Workshop on Silicon Heterojunction Solar Cells, 2022.
[39] Canadian Solar, Canadian Solar To Start Mass Production Of Topcon Modules With Power Output Up To 690w, (2022). http://investors.canadiansolar.com/news-releases/news-release-details/canadian-solar-start-mass-production-topcon-modules-power-output#:~:text=Canadian Solar's TOPCon modules are, mainstream products in the market.
[40] C. Battaglia, X. Yin, M. Zheng, I.D. Sharp, T. Chen, S. McDonnell, A. Azcatl, C. Carraro, B. Ma, R. Maboudian, R.M. Wallace, A. Javey, Hole selective MoO x contact for silicon solar cells, Nano Lett. 14 (2014) 967–971, https://doi.org/10.1021/nl404389u.
[41] J. Bullock, A. Cuevas, T. Allen, C. Battaglia, Molybdenum oxide MoOx: a versatile hole contact for silicon solar cells, Appl. Phys. Lett. 105 (2014), 232109, https://doi.org/10.1063/1.4903467.
[42] J. Geissbühler, J. Werner, S. Martin de Nicolas, L. Barraud, A. Hessler-Wyser, M. Despeisse, S. Nicolay, A. Tomasi, B. Niesen, S. De Wolf, C. Ballif, 22.5% efficient silicon heterojunction solar cell with molybdenum oxide hole collector, Appl. Phys. Lett. 107 (2015), 81601, https://doi.org/10.1063/1.4928747.
[43] J. Dréon, Q. Jeangros, J. Cattin, J. Haschke, L. Antognini, C. Ballif, M. Boccard, 23.5%-efficient silicon heterojunction silicon solar cell using molybdenum oxide as hole-selective contact, Nano Energy 70 (2020), 104495, https://doi.org/10.1016/j.nanoen.2020.104495.
[44] M. Bivour, J. Temmler, H. Steinkemper, M. Hermle, Molybdenum and tungsten oxide: high work function wide band gap contact materials for hole selective contacts of silicon solar cells, Sol. Energy Mater. Sol. Cells 142 (2015) 34–41, https://doi.org/10.1016/j.solmat.2015.05.031.
[45] M. Mews, L. Korte, B. Rech, Oxygen vacancies in tungsten oxide and their influence on tungsten oxide/silicon heterojunction solar cells, Sol. Energy Mater. Sol. Cells 158 (2016) 77–83, https://doi.org/10.1016/j.solmat.2016.05.042.
[46] X. Yang, H. Xu, W. Liu, Q. Bi, L. Xu, J. Kang, M.N. Hedhili, B. Sun, X. Zhang, S. De Wolf, Atomic layer deposition of vanadium oxide as hole-selective contact for crystalline silicon solar cells, Adv. Electron. Mater. 6 (2020), 2000467, https://doi.org/10.1002/aelm.202000467.
[47] J. Bullock, M. Hettick, J. Geissbühler, A.J. Ong, T. Allen, C.M. Sutter-Fella, T. Chen, H. Ota, E.W. Schaler, S. De Wolf, C. Ballif, A. Cuevas, A. Javey, Efficient

silicon solar cells with dopant-free asymmetric heterocontacts, Nat. Energy 1 (2016) 1–7, https://doi.org/10.1038/nenergy.2015.31.
[48] G. Chistiakova, B. Macco, L. Korte, Low-temperature atomic layer deposited magnesium oxide as a passivating electron contact for c-Si-based solar cells, IEEE J. Photovoltaics 10 (2020) 398–406, https://doi.org/10.1109/JPHOTOV.2019.2961603.
[49] Y. Wan, C. Samundsett, J. Bullock, T. Allen, M. Hettick, D. Yan, P. Zheng, X. Zhang, J. Cui, J. McKeon, A. Javey, A. Cuevas, Magnesium fluoride electron-selective contacts for crystalline silicon solar cells, ACS Appl. Mater. Interfaces 8 (2016) 14671–14677, https://doi.org/10.1021/acsami.6b03599.
[50] S. Avasthi, W.E. McClain, G. Man, A. Kahn, J. Schwartz, J.C. Sturm, Hole-blocking titanium-oxide/silicon heterojunction and its application to photovoltaics, Appl. Phys. Lett. 102 (2013), 203901, https://doi.org/10.1063/1.4803446.
[51] X. Yang, P. Zheng, Q. Bi, K. Weber, Silicon heterojunction solar cells with electron selective TiOx contact, Sol. Energy Mater. Sol. Cells 150 (2016) 32–38, https://doi.org/10.1016/j.solmat.2016.01.020.
[52] W. Wang, L. Cai, L. Meng, N. Chen, H. Wei, Y. Hong, Y. Chen, L. Zeng, Z. Liang, Highly Stable Strontium Fluoride as a Thickness Tolerant Electron-Selective Contact for Dopant-Free Silicon Solar Cells, 2023, https://doi.org/10.22541/au.168023523.37894824/v1.
[53] T.G. Allen, J. Bullock, X. Yang, A. Javey, S. De Wolf, Passivating contacts for crystalline silicon solar cells, Nat. Energy 4 (2019) 914–928, https://doi.org/10.1038/s41560-019-0463-6.
[54] L. Cao, P. Procel, A. Alcañiz, J. Yan, F. Tichelaar, E. Özkol, Y. Zhao, C. Han, G. Yang, Z. Yao, M. Zeman, R. Santbergen, L. Mazzarella, O. Isabella, Achieving 23.83% conversion efficiency in silicon heterojunction solar cell with ultra-thin MoOx hole collector layer via tailoring (i)a-Si: H/MoOx interface, Prog. Photovoltaics Res. Appl. (2022), https://doi.org/10.1002/pip.3638.
[55] S. Zhong, J. Dreon, Q. Jeangros, E. Aydin, S. De Wolf, F. Fu, M. Boccard, C. Ballif, Mitigating plasmonic absorption losses at rear electrodes in high-efficiency silicon solar cells using dopant-free contact stacks, Adv. Funct. Mater. 30 (2020), 1907840, https://doi.org/10.1002/adfm.201907840.
[56] J. Bullock, Y. Wan, Z. Xu, S. Essig, M. Hettick, H. Wang, W. Ji, M. Boccard, A. Cuevas, C. Ballif, Stable dopant-free asymmetric heterocontact silicon solar cells with efficiencies above 20, ACS Energy Lett. 3 (2018) 508–513, https://doi.org/10.1021/acsenergylett.7b01279.
[57] J. Cho, N. Nawal, A. Hadipour, M.R. Payo, A. van der Heide, H.S. Radhakrishnan, M. Debucquoy, I. Gordon, J. Szlufcik, J. Poortmans, Interface analysis and intrinsic thermal stability of MoOx based hole-selective contacts for silicon heterojunction solar cells, Sol. Energy Mater. Sol. Cells 201 (2019), 110074, https://doi.org/10.1016/j.solmat.2019.110074.
[58] J. Cho, H.S. Radhakrishnan, R. Sharma, M.R. Payo, M. Debucquoy, A. van der Heide, I. Gordon, J. Szlufcik, J. Poortmans, Thermal stability improvement of metal oxide-based contacts for silicon heterojunction solar cells, Sol. Energy Mater. Sol. Cells 206 (2020), 110324, https://doi.org/10.1016/j.solmat.2019.110324.
[59] Vdma, International Technology Roadmap for Photovoltaic, fourteenth ed., 2023.
[60] NREL, Best Research-Cell Efficiency Chart. https://www.nrel.gov/pv/interactive-cell-efficiency.html, 2023. (Accessed 31 May 2023).
[61] L. Senaud, B. Kamino, J. Geissbühler, G. Christmann, G. Nogay, J. Zhao, F. Sahli, P. Wyss, D.L. Bätzner, D. Lachenal, Q. Jeangros, C. Ballif, B. Paviet-Salomon, High Efficiency 3-Terminal Perovskite/Silicon Tandems Based on Tunnel Junction IBC, the 8th World Conference on Photovoltaic Energy Conversion, Milan, 2022.
[62] K. Yamamoto, H. Uzu, D. Adachi, High efficiency perovskite/hetero-junction crystalline silicon tandem solar cells, in: The 33rd International Photovoltaic Science and Engineering Conference, Nagoya, 2022.
[63] J. Werner, B. Niesen, C. Ballif, Perovskite/silicon tandem solar cells: marriage of convenience or true love story? – An overview, Adv. Mater. Interfac. 5 (2018) 1–19, https://doi.org/10.1002/admi.201700731.
[64] F. Fu, J. Li, T.C. Yang, H. Liang, A. Faes, Q. Jeangros, C. Ballif, Y. Hou, Monolithic perovskite-silicon tandem solar cells: from the lab to fab? Adv. Mater. 34 (2022), 2106540 https://doi.org/10.1002/adma.202106540.
[65] P. Tockhorn, J. Sutter, A. Cruz, P. Wagner, K. Jäger, D. Yoo, F. Lang, M. Grischek, B. Li, J. Li, O. Shargaieva, E. Unger, A. Al-Ashouri, E. Köhnen, M. Stolterfoht, D. Neher, R. Schlatmann, B. Rech, B. Stannowski, S. Albrecht, C. Becker, Nano-optical designs for high-efficiency monolithic perovskite–silicon tandem solar cells, Nat. Nanotechnol. (2022) 1–8, https://doi.org/10.1038/s41565-022-01228-8.
[66] E. Raza, Z. Ahmad, Review on two-terminal and four-terminal crystalline-silicon/perovskite tandem solar cells; progress, challenges, and future perspectives, Energy Rep. 8 (2022) 5820–5851, https://doi.org/10.1016/j.egyr.2022.04.028.
[67] T. Dullweber, H. Hannebauer, U. Baumann, T. Falcon, K. Bothe, S. Steckemetz, R. Brendel, Fine-line printed 5 busbar PERC solar cells with conversion efficiencies beyond 21, in: 29th EU PV Sol. Energy Conf., 2014, p. 621, https://doi.org/10.4229/EUPVSEC20142014-2DO.3.4.
[68] A. Richter, R. Müller, J. Benick, F. Feldmann, B. Steinhauser, C. Reichel, A. Fell, M. Bivour, M. Hermle, S.W. Glunz, Design rules for high-efficiency both-sides-contacted silicon solar cells with balanced charge carrier transport and recombination losses, Nat. Energy 6 (2021) 429–438, https://doi.org/10.1038/s41560-021-00805-w.
[69] C. Ballif, F.-J. Haug, M. Boccard, P.J. Verlinden, G. Hahn, Status and perspectives of crystalline silicon photovoltaics in research and industry, Nat. Rev. Mater. 7 (2022) 597–616, https://doi.org/10.1038/s41578-022-00423-2.
[70] F. Feldmann, M. Simon, M. Bivour, C. Reichel, M. Hermle, S.W. Glunz, Efficient carrier-selective p- and n-contacts for Si solar cells, Sol. Energy Mater. Sol. Cells 131 (2014) 100–104, https://doi.org/10.1016/j.solmat.2014.05.039.
[71] M. Taguchi, K. Kawamoto, S. Tsuge, T. Baba, H. Sakata, M. Morizane, K. Uchihashi, N. Nakamura, S. Kiyama, O. Oota, HITTM cells—high-efficiency crystalline Si cells with novel structure, Prog. Photovoltaics Res. Appl. 8 (2000) 503–513, https://doi.org/10.1002/1099-159X(200009/10)8:5%3C503::AID-PIP347%3E3.0.CO;2-G.
[72] H. Sakala, T. Nakai, T. Babe, M. Tajuchi, S. Tsuge, K. Uchihashi, S. Klyama, 20.7% highest efficiency large area (100.5 cm2) HITTM cell, in: 28th IEEE PVSC, 2000, pp. 7–12, https://doi.org/10.1109/PVSC.2000.915742.
[73] M. Taguchi, A. Terakawa, E. Maruyama, M. Tanaka, Obtaining a higher Voc in HIT cells, Prog. Photovoltaics Res. Appl. 13 (2005) 481–488, https://doi.org/10.1002/pip.646.
[74] Y. Tsunomura, Y. Yoshimine, M. Taguchi, T. Baba, T. Kinoshita, H. Kanno, H. Sakata, E. Maruyama, M. Tanaka, Twenty-two percent efficiency HIT solar cell, Sol. Energy Mater. Sol. Cells 93 (2009) 670–673, https://doi.org/10.1016/j.solmat.2008.02.037.
[75] T. Mishima, M. Taguchi, H. Sakata, E. Maruyama, Development status of high-efficiency HIT solar cells, Sol. Energy Mater. Sol. Cells 95 (2011) 18–21, https://doi.org/10.1016/j.solmat.2010.04.030.
[76] T. Kinoshita, D. Fujishima, A. Yano, A. Ogane, S. Tohoda, K. Matsuyama, Y. Nakamura, N. Tokuoka, H. Kanno, H. Sakata, M. Taguchi, E. Maruyama, The approaches for high efficiency HITTM solar cell with very thin (<100 μm) silicon wafer over 23, in: 26th Eur. Photovolt. Sol. Energy Conf. Exhib, 2011, pp. 871–874, https://doi.org/10.4229/26thEUPVSEC2011-2AO.2.6.
[77] S. De Wolf, A. Descoeudres, Z.C. Holman, C. Ballif, High-efficiency silicon heterojunction solar cells: a review, Greenpeace 2 (2012), https://doi.org/10.1515/green-2011-0018.
[78] W. van Sark, L. Korte, F. Roca, Physics and Technology of Amorphous-Crystalline Heterostructure Silicon Solar Cells, Springer, 2012, https://doi.org/10.1007/978-3-642-22275-7.
[79] C. Ballif, S. De Wolf, A. Descoeudres, Z.C. Holman, Amorphous silicon/crystalline silicon heterojunction solar cells, in: Semicond. Semimetals, Elsevier, 2014, pp. 73–120, https://doi.org/10.1016/B978-0-12-388417-6.00003-9.
[80] S. Noguchi, H. Iwata, K. Sano, Photovoltaic Device, US5213628A, 1993.
[81] M. Taguchi, A. Yano, S. Tohoda, K. Matsuyama, Y. Nakamura, T. Nishiwaki, K. Fujita, E. Maruyama, 24.7% Record efficiency HIT solar cell on thin silicon wafer, IEEE J. Photovoltaics 4 (2014) 96–99, https://doi.org/10.1109/JPHOTOV.2013.2282737.
[82] K. Masuko, M. Shigematsu, T. Hashiguchi, D. Fujishima, M. Kai, N. Yoshimura, T. Yamaguchi, Y. Ichihashi, T. Mishima, N. Matsubara, T. Yamanishi, T. Takahama, M. Taguchi, E. Maruyama, S. Okamoto, Achievement of more than 25% conversion efficiency with crystalline silicon heterojunction solar cell, IEEE J. Photovoltaics 4 (2014) 1433–1435, https://doi.org/10.1109/JPHOTOV.2014.2352151.
[83] D. Adachi, J.L. Hernández, K. Yamamoto, Impact of carrier recombination on fill factor for large area heterojunction crystalline silicon solar cell with 25.1% efficiency, Appl. Phys. Lett. 107 (2015), 233506, https://doi.org/10.1063/1.4937224.
[84] LONGi Solar, at 26.81%, LONGi Sets a New World Record Efficiency for Silicon Solar Cells, 2022. https://www.longi.com/en/news/propelling-the-transformation/.
[85] S.K. Chunduri, M. Schmela, Heterojunction Solar Technology 2023 - Working Hard on Cost Reduction, 2023.
[86] R.V.K. Chavali, S. De Wolf, M.A. Alam, Device physics underlying silicon heterojunction and passivating-contact solar cells: a topical review, Prog. Photovoltaics Res. Appl. (2018) 1–20, https://doi.org/10.1002/pip.2959.
[87] Z. Sun, X. Chen, Y. He, J. Li, J. Wang, H. Yan, Y. Zhang, Toward efficiency limits of crystalline silicon solar cells: recent progress in high-efficiency silicon heterojunction solar cells, Adv. Energy Mater. 12 (2022), 2200015, https://doi.org/10.1002/aenm.202200015.
[88] J. Haschke, O. Dupré, M. Boccard, C. Ballif, Silicon heterojunction solar cells : recent technological development and practical aspects - from lab to industry, Sol. Energy Mater. Sol. Cells 187 (2018) 140–153, https://doi.org/10.1016/j.solmat.2018.07.018.
[89] Y. Liu, Y. Li, Y. Wu, G. Yang, L. Mazzarella, P. Procel-Moya, A.C. Tamboli, K. Weber, M. Boccard, O. Isabella, X. Yang, B. Sun, High-efficiency silicon heterojunction solar cells: materials, devices and applications, Mater. Sci. Eng. R Rep. 142 (2020), 100579, https://doi.org/10.1016/j.mser.2020.100579.
[90] A. Razzaq, T.G. Allen, W. Liu, Z. Liu, S. De Wolf, Silicon heterojunction solar cells: techno-economic assessment and opportunities, Joule 6 (2022) 514–542, https://doi.org/10.1016/j.joule.2022.02.009.
[91] Y. Zhang, M. Kim, L. Wang, P. Verlinden, B. Hallam, Design considerations for multi-terawatt scale manufacturing of existing and future photovoltaic technologies: challenges and opportunities related to silver, indium and bismuth consumption, Energy Environ. Sci. 14 (2021) 5587–5610, https://doi.org/10.1039/D1EE01814K.
[92] P.V. Magazine, Huasun Achieves 25.26% Efficiency for Heterojunction Solar Cell, 2021. https://www.pv-magazine.com/2021/07/13/huasun-achieves-25-26-efficiency-for-heterojunction-solar-cell/. (Accessed 31 March 2023).
[93] M. Yang, X. Ru, S. Yin, C. Hong, F. Peng, M. Qu, J. Lu, L. Fang, X. Xu, Over 26% efficiency SHJ solar cell using nanocrystalline silicon oxide window layer, in: The 8th World Conference on Photovoltaic Energy Conversion, WCPEC-8), Milan, 2022.
[94] X. Ru, M. Qu, J. Wang, T. Ruan, M. Yang, F. Peng, W. Long, K. Zheng, H. Yan, X. Xu, 25.11% efficiency silicon heterojunction solar cell with low deposition rate intrinsic amorphous silicon buffer layers, Sol. Energy Mater. Sol. Cells 215 (2020), 110643, https://doi.org/10.1016/j.solmat.2020.110643.

[95] T. Sawada, N. Terada, S. Tsuge, T. Baba, T. Takahama, K. Wakisaka, S. Tsuda, S. Nakano, High-efficiency of a-Si/c-Si heterojunction solar cell, WCPEC-1 2 (1994) 1219–1226, https://doi.org/10.1109/WCPEC.1994.519952.
[96] G. Yang, P. Guo, P. Procel, G. Limodio, A. Weeber, O. Isabella, M. Zeman, High-efficiency black IBC c-Si solar cells with poly-Si as carrier-selective passivating contacts, Sol. Energy Mater. Sol. Cells 186 (2018) 9–13, https://doi.org/10.1016/j.solmat.2018.06.019.
[97] D. Deligiannis, S. Alivizatos, A. Ingenito, D. Zhang, M. van Sebille, R.A.C.M. M. van Swaaij, M. Zeman, Wet-chemical treatment for improved surface passivation of textured silicon heterojunction solar cells, Energy Proc. 55 (2014) 197–202, https://doi.org/10.1016/j.egypro.2014.08.117.
[98] Synopsis, Sentaurus Device User, 2013.
[99] R. Santbergen, T. Meguro, T. Suezaki, G. Koizumi, K. Yamamoto, M. Zeman, GenPro4 optical model for solar cell simulation and its application to multijunction solar cells, IEEE J. Photovoltaics 7 (2017) 919–926, https://doi.org/10.1109/JPHOTOV.2017.2669640.
[100] G. Kresse, J. Furthmüller, Efficient iterative schemes for ab initio total-energy calculations using a plane-wave basis set, Phys. Rev. B 54 (1996), 11169, https://doi.org/10.1103/PhysRevB.54.11169.
[101] G. Kresse, D. Joubert, From ultrasoft pseudopotentials to the projector augmented-wave method, Phys. Rev. B 59 (1999) 1758, https://doi.org/10.1103/PhysRevB.59.1758.
[102] P. Procel, G. Yang, O. Isabella, M. Zeman, Theoretical evaluation of contact stack for high efficiency IBC-SHJ solar cells, Sol. Energy Mater. Sol. Cells 186 (2018) 66–77, https://doi.org/10.1016/j.solmat.2018.06.021.
[103] P. Procel, H. Xu, A. Saez, C. Ruiz-Tobon, L. Mazzarella, Y. Zhao, C. Han, G. Yang, M. Zeman, O. Isabella, The role of heterointerfaces and subgap energy states on transport mechanisms in silicon heterojunction solar cells, Prog. Photovoltaics Res. Appl. 28 (2020) 935–945, https://doi.org/10.1002/pip.3300.
[104] T.F. Schulze, L. Korte, F. Ruske, B. Rech, Band lineup in amorphous/crystalline silicon heterojunctions and the impact of hydrogen microstructure and topological disorder, Phys. Rev. B 83 (2011), 165314, https://doi.org/10.1103/PhysRevB.83.165314.
[105] U. Wurfel, A. Cuevas, P. Wurfel, Charge carrier separation in solar cells, IEEE J. Photovoltaics 5 (2015) 461–469, https://doi.org/10.1109/JPHOTOV.2014.2363550.
[106] A. Cuevas, T. Allen, J. Bullock, Y. Wan, D. Yan, X. Zhang, Skin care for healthy silicon solar cells, in: 2015 IEEE 42nd Photovolt. Spec. Conf., IEEE, 2015, pp. 1–6, https://doi.org/10.1109/PVSC.2015.7356379.
[107] T.F. Schulze, L. Korte, E. Conrad, M. Schmidt, B. Rech, Electrical transport mechanisms in a-Si: H/c-Si heterojunction solar cells, J. Appl. Phys. 107 (2010), 23711, https://doi.org/10.1063/1.3267316.
[108] L. Zhao, C.L. Zhou, H.L. Li, H.W. Diao, W.J. Wang, Design optimization of bifacial HIT solar cells on p-type silicon substrates by simulation, Sol. Energy Mater. Sol. Cells 92 (2008) 673–681, https://doi.org/10.1016/j.solmat.2008.01.018.
[109] K.U. Ritzau, M. Bivour, S. Schröer, H. Steinkemper, P. Reinecke, F. Wagner, M. Hermle, TCO work function related transport losses at the a-Si:H/TCO-contact in SHJ solar cells, Sol. Energy Mater. Sol. Cells 131 (2014) 9–13, https://doi.org/10.1016/j.solmat.2014.06.026.
[110] M. Bivour, S. Schröer, M. Hermle, Numerical analysis of electrical TCO/a-Si:H(p) contact properties for silicon heterojunction solar cells, Energy Proc. 38 (2013) 658–669, https://doi.org/10.1016/j.egypro.2013.07.330.
[111] G. Nogay, J.P. Seif, Y. Riesen, A. Tomasi, Q. Jeangros, N. Wyrsch, F.-J. Haug, S. De Wolf, C. Ballif, Nanocrystalline silicon carrier collectors for silicon heterojunction solar cells and impact on low-temperature device characteristics, IEEE J. Photovoltaics 6 (2016) 1654–1662, https://doi.org/10.1109/JPHOTOV.2016.2604574.
[112] D. Lachenal, P. Papet, B. Legradic, R. Kramer, T. Kössler, L. Andreetta, N. Holm, W. Frammelsberger, D.L. Baetzner, B. Strahm, L.L. Senaud, J.W. Schüttauf, A. Descoeudres, G. Christmann, S. Nicolay, M. Despeisse, B. Paviet-Salomon, C. Ballif, Optimization of tunnel-junction IBC solar cells based on a series resistance model, Sol. Energy Mater. Sol. Cells 200 (2019), 110036, https://doi.org/10.1016/j.solmat.2019.110036.
[113] D.K. Schroder, D.L. Meier, Solar cell contact resistance—a review, IEEE Trans. Electron. Dev. 31 (1984) 637–647, https://doi.org/10.1109/T-ED.1984.21583.
[114] D. Lachenal, D. Baetzner, W. Frammelsberger, B. Legradic, J. Meixenberger, P. Papet, B. Strahm, G. Wahli, Heterojunction and passivated contacts: a simple method to extract both n/tco and p/tco contacts resistivity, Energy Proc. 92 (2016) 932–938, https://doi.org/10.1016/j.egypro.2016.07.104.
[115] P. Procel Moya, H. Xu, L. Mazzarella, L.-L. Senaud, B. Paviet-Salomon, H. Sivaramakrishnan Radhakrishna, M. Filipic, M. Xu, M. Boccard, A. Fioretti, R. Monnard, J.-C. Stang, P. Wagner, D. Meza, D. Lachenal, B. Strahm, W. Duan, A. Lambertz, A. Fejfar, K. Ding, M. Despeisse, I. Gordon, L. Korte, C. Ballif, O. Isabella, M. Zeman, On the correlation between contact resistivity and high efficiency in (IBC-) SHJ solar cells, in: 36th Eur. Photovolt. Sol. Energy Conf. Exhib., 2019, pp. 251–254, https://doi.org/10.4229/EUPVSEC20192019-2CO.12.6.
[116] D. Deligiannis, R. Vasudevan, A.H.M. Smets, R.A. van Swaaij, M. Zeman, Surface passivation of c-Si for silicon heterojunction solar cells using high-pressure hydrogen diluted plasmas, AIP Adv. 5 (2015), 97165, https://doi.org/10.1063/1.4931821.
[117] J. Ge, Z.P. Ling, J. Wong, T. Mueller, a.G. Aberle, Optimisation of intrinsic a-Si:H passivation layers in crystalline-amorphous silicon heterojunction solar cells, Energy Proc. 15 (2012) 107–117, https://doi.org/10.1016/j.egypro.2012.02.013.
[118] Y. Zhao, P. Procel, A. Smets, L. Mazzarella, C. Han, G. Yang, L. Cao, Z. Yao, A. Weeber, M. Zeman, Effects of (i)a-Si: H deposition temperature on high-efficiency silicon heterojunction solar cells, Prog. Photovoltaics Res. Appl. (2022), https://doi.org/10.1002/pip.3620.
[119] S.-K. Kim, J.C. Lee, S.-J. Park, Y.-J. Kim, K.H. Yoon, Effect of hydrogen dilution on intrinsic a-Si: H layer between emitter and Si wafer in silicon heterojunction solar cell, Sol. Energy Mater. Sol. Cells 92 (2008) 298–301, https://doi.org/10.1016/j.solmat.2007.09.007.
[120] A. Descoeudres, L. Barraud, R. Bartlome, G. Choong, S. De Wolf, F. Zicarelli, C. Ballif, The silane depletion fraction as an indicator for the amorphous/crystalline silicon interface passivation quality, Appl. Phys. Lett. 97 (2010) 1–4, https://doi.org/10.1063/1.3511737.
[121] H. Sai, H.-J. Hsu, P.-W. Chen, P.-L. Chen, T. Matsui, Intrinsic amorphous silicon bilayers for effective surface passivation in silicon heterojunction solar cells: a comparative study of interfacial layers, Phys. Status Solidi 218 (2021), 2000743, https://doi.org/10.1002/pssa.202000743.
[122] K.-S. Lee, C.B. Yeon, S.J. Yun, K.H. Jung, J.W. Lim, Improved surface passivation using dual-layered a-Si: H for silicon heterojunction solar cells, ECS Solid State Lett 3 (2014) P33, https://doi.org/10.1149/2.001404ssl.
[123] Y. Zhang, C. Yu, M. Yang, L.-R. Zhang, Y.-C. He, J.-Y. Zhang, X.-X. Xu, Y.-Z. Zhang, X.-M. Song, H. Yan, Significant improvement of passivation performance by two-step preparation of amorphous silicon passivation layers in silicon heterojunction solar cells, Chin. Phys. Lett. 34 (2017), 038101, https://doi.org/10.1088/0256-307X/34/3/038101.
[124] W. Liu, L. Zhang, R. Chen, F. Meng, W. Guo, J. Bao, Z. Liu, Underdense a-Si: H film capped by a dense film as the passivation layer of a silicon heterojunction solar cell, J. Appl. Phys. 120 (2016), 175301, https://doi.org/10.1063/1.4966941.
[125] F.A. Bin Mohd Zulkifly, Y. Shiratori, K. Nakada, S. Miyajima, Impact of bilayer structures on the surface passivation quality of high-rate-sputtered hydrogenated amorphous silicon for silicon heterojunction solar cells, Prog. Photovoltaics Res. Appl. 28 (2020) 971–976, https://doi.org/10.1002/pip.3298.
[126] X. Qu, Y. He, M. Qu, T. Ruan, F. Chu, Z. Zheng, Y. Ma, Y. Chen, X. Ru, X. Xu, H. Yan, L. Wang, Y. Zhang, X. Hao, Z. Hameiri, Z.-G. Chen, L. Wang, K. Zheng, Identification of embedded nanotwins at c-Si/a-Si:H interface limiting the performance of high-efficiency silicon heterojunction solar cells, Nat. Energy 6 (2021) 194–202, https://doi.org/10.1038/s41560-020-00768-4.
[127] H. Sai, P.-W. Chen, H.-J. Hsu, T. Matsui, S. Nunomura, K. Matsubara, Impact of intrinsic amorphous silicon bilayers in silicon heterojunction solar cells, J. Appl. Phys. 124 (2018), 103102.
[128] M. Mews, T.F. Schulze, N. Mingirulli, L. Korte, Hydrogen plasma treatments for passivation of amorphous-crystalline silicon-heterojunctions on surfaces promoting epitaxy, Appl. Phys. Lett. 102 (2013), https://doi.org/10.1063/1.4798292.
[129] A. Neumüller, O. Sergeev, S.J. Heise, S. Bereznev, O. Volobujeva, J.F.L. Salas, M. Vehse, C. Agert, Improved amorphous silicon passivation layer for heterojunction solar cells with post-deposition plasma treatment, Nano Energy 43 (2018) 228–235, https://doi.org/10.1016/j.nanoen.2017.11.053.
[130] A. Descoeudres, L. Barraud, S. De Wolf, B. Strahm, D. Lachenal, C. Guérin, Z. C. Holman, F. Zicarelli, B. Demaurex, J. Seif, J. Holovsky, C. Ballif, Improved amorphous/crystalline silicon interface passivation by hydrogen plasma treatment, Appl. Phys. Lett. 99 (2011) 1–4, https://doi.org/10.1063/1.3641899.
[131] Y. Zhao, L. Mazzarella, P. Procel, C. Han, G. Yang, A. Weeber, M. Zeman, O. Isabella, Doped hydrogenated nanocrystalline silicon oxide layers for high-efficiency c-Si heterojunction solar cells, Prog. Photovoltaics Res. Appl. 28 (2020), https://doi.org/10.1002/pip.3256.
[132] L. Zhang, W. Guo, W. Liu, J. Bao, J. Liu, J. Shi, F. Meng, Z. Liu, Investigation of positive roles of hydrogen plasma treatment for interface passivation based on silicon heterojunction solar cells, J. Phys. D Appl. Phys. 49 (2016), 165305, https://doi.org/10.1088/0022-3727/49/16/165305.
[133] A. Soman, U. Nsofor, U. Das, T. Gu, S. Hegedus, Correlation between in situ diagnostics of the hydrogen plasma and the interface passivation quality of hydrogen plasma post-treated a-Si: H in silicon heterojunction solar cells, ACS Appl. Mater. Interfaces 11 (2019) 16181–16190, https://doi.org/10.1021/acsami.9b01686.
[134] M. Xu, C. Wang, T. Bearda, E. Simoen, H.S. Radhakrishnan, I. Gordon, W. Li, J. Szlufcik, J. Poortmans, Dry passivation process for silicon heterojunction solar cells using hydrogen plasma treatment followed by in situ a-Si: H deposition, IEEE J. Photovoltaics 8 (2018) 1539–1545, https://doi.org/10.1109/JPHOTOV.2018.2871329.
[135] F. Wang, X. Zhang, L. Wang, Y. Jiang, C. Wei, S. Xu, Y. Zhao, Improved amorphous/crystalline silicon interface passivation for heterojunction solar cells by low-temperature chemical vapor deposition and post-annealing treatment, Phys. Chem. Chem. Phys. 16 (2014) 20202–20208, https://doi.org/10.1039/c4cp02212b.
[136] S. De Wolf, M. Kondo, Abruptness of a-Si:H/c-Si interface revealed by carrier lifetime measurements, Appl. Phys. Lett. 90 (2007) 1–4, https://doi.org/10.1063/1.2432297.
[137] S. Dauwe, J. Schmidt, R. Hezel, Very low surface recombination velocities on p- and n-type silicon wafers passivated with hydrogenated amorphous silicon films, in: Conf. Rec. Twenty-Ninth IEEE Photovolt. Spec. Conf. 2002, IEEE, 2002, pp. 1246–1249, https://doi.org/10.1109/PVSC.2002.1190834.
[138] B. Macco, J. Melskens, N.J. Podraza, K. Arts, C. Pugh, O. Thomas, W.M.M. Kessels, Correlating the silicon surface passivation to the nanostructure of low-temperature a-Si: H after rapid thermal annealing, J. Appl. Phys. 122 (2017), 35302, https://doi.org/10.1063/1.4994795.
[139] M.Z. Burrows, U.K. Das, R.L. Opila, S. De Wolf, R.W. Birkmire, Role of hydrogen bonding environment in a-Si:H films for c-Si surface passivation, J. Vac. Sci.

Technol. A Vacuum, Surfaces, Film. 26 (2008) 683–687, https://doi.org/10.1116/1.2897929.
[140] L. V Mercaldo, E. Bobeico, I. Usatii, M. Della Noce, L. Lancellotti, L. Serenelli, M. Izzi, M. Tucci, P.D. Veneri, Potentials of mixed-phase doped layers in p-type Si heterojunction solar cells with ZnO: Al, Sol. Energy Mater. Sol. Cells 169 (2017) 113–121, https://doi.org/10.1016/j.solmat.2017.05.014.
[141] H. Umishio, H. Sai, T. Koida, T. Matsui, Nanocrystalline-silicon hole contact layers enabling efficiency improvement of silicon heterojunction solar cells: impact of nanostructure evolution on solar cell performance, Prog. Photovoltaics Res. Appl. 29 (2021) 344–356, https://doi.org/10.1002/pip.3368.
[142] Y. Zhao, L. Mazzarella, P. Procel, C. Han, F.D. Tichelaar, G. Yang, A. Weeber, M. Zeman, O. Isabella, Ultra-thin electron collectors based on nc-Si: H for high-efficiency silicon heterojunction solar cells, Prog. Photovoltaics Res. Appl. 30 (2022) 809–822, https://doi.org/10.1002/pip.3502.
[143] S. De Wolf, M. Kondo, Surface passivation properties of stacked doped PECVD a-Si: H layers for hetero-structure c-Si solar cells, in: 2006 IEEE 4th World Conf. Photovolt. Energy Conf., IEEE, 2006, pp. 1469–1472, https://doi.org/10.1109/WCPEC.2006.279746.
[144] S. De Wolf, M. Kondo, Boron-doped a-Si:H/c-Si interface passivation: degradation mechanism, Appl. Phys. Lett. 91 (2007), 112109, https://doi.org/10.1063/1.2783972.
[145] S. De Wolf, M. Kondo, Nature of doped a-Si:H/c-Si interface recombination, J. Appl. Phys. 105 (2009), 103707, https://doi.org/10.1063/1.3129578.
[146] T.F. Schulze, C. Leendertz, N. Mingirulli, L. Korte, B. Rech, Impact of Fermi-level dependent defect equilibration on Voc of amorphous/crystalline silicon heterojunction solar cells, Energy Proc. 8 (2011) 282–287, https://doi.org/10.1016/j.egypro.2011.06.137.
[147] Z. Wu, L. Zhang, W. Liu, R. Chen, Z. Li, F. Meng, Z. Liu, Role of hydrogen in modifying a-Si: H/c-Si interface passivation and band alignment for rear-emitter silicon heterojunction solar cells, J. Mater. Sci. Mater. Electron. 31 (2020) 9468–9474, https://doi.org/10.1007/s10854-020-03486-5.
[148] C. Luderer, D. Kurt, A. Moldovan, M. Hermle, M. Bivour, Intrinsic layer modification in silicon heterojunctions: balancing transport and surface passivation, Sol. Energy Mater. Sol. Cells 238 (2022), 111412, https://doi.org/10.1016/j.solmat.2021.111412.
[149] R.A. Street, C.C. Tsai, J. Kakalios, W.B. Jackson, Hydrogen diffusion in amorphous silicon, Philos. Mag. B 56 (1987) 305–320, https://doi.org/10.1080/13642818708221319.
[150] W. Beyer, Hydrogen effusion: a probe for surface desorption and diffusion, Phys. B Condens. Matter 170 (1991) 105–114, https://doi.org/10.1016/0921-4526(91)90111-Q.
[151] J. Geissbühler, S. De Wolf, B. Demaurex, J.P. Seif, D.T.L. Alexander, L. Barraud, C. Ballif, Amorphous/crystalline silicon interface defects induced by hydrogen plasma treatments, Appl. Phys. Lett. 102 (2013), https://doi.org/10.1063/1.4811253.
[152] L. Mazzarella, S. Kirner, B. Stannowski, L. Korte, B. Rech, R. Schlatmann, p-type microcrystalline silicon oxide emitter for silicon heterojunction solar cells allowing current densities above 40 mA/cm2, Appl. Phys. Lett. 106 (2015), 23902, https://doi.org/10.1063/1.4905906.
[153] A. Lambertz, V. Smirnov, T. Merdzhanova, K. Ding, S. Haas, G. Jost, R.E. I. Schropp, F. Finger, U. Rau, Microcrystalline silicon–oxygen alloys for application in silicon solar cells and modules, Sol. Energy Mater. Sol. Cells 119 (2013) 134–143, https://doi.org/10.1016/j.solmat.2013.05.053.
[154] K. Nakada, S. Miyajima, M. Konagai, Application of n-type microcrystalline silicon oxide as back reflector of crystalline silicon heterojunction solar cells, Jpn. J. Appl. Phys. 54 (2015), 82301, https://doi.org/10.7567/JJAP.54.082301.
[155] A. Richter, V. Smirnov, A. Lambertz, K. Nomoto, K. Welter, K. Ding, Versatility of doped nanocrystalline silicon oxide for applications in silicon thin-film and heterojunction solar cells, Sol. Energy Mater. Sol. Cells 174 (2018) 196–201, https://doi.org/10.1016/j.solmat.2017.08.035.
[156] D. Qiu, W. Duan, A. Lambertz, K. Bittkau, P. Steuter, Y. Liu, A. Gad, M. Pomaska, U. Rau, K. Ding, Front contact optimization for rear-junction SHJ solar cells with ultra-thin n-type nanocrystalline silicon oxide, Sol. Energy Mater. Sol. Cells 209 (2020), 110471, https://doi.org/10.1016/j.solmat.2020.110471.
[157] K. Ding, U. Aeberhard, F. Finger, U. Rau, Silicon heterojunction solar cell with amorphous silicon oxide buffer and microcrystalline silicon oxide contact layers, Phys. Status Solidi Rapid Res. Lett. 6 (2012) 193–195, https://doi.org/10.1002/pssr.201206030.
[158] S. Kirner, L. Mazzarella, L. Korte, B. Stannowski, B. Rech, R. Schlatmann, Silicon heterojunction solar cells with nanocrystalline silicon oxide emitter: insights into charge carrier transport, IEEE J. Photovoltaics 5 (2015) 1601–1605, https://doi.org/10.1109/JPHOTOV.2015.2479461.
[159] J. Haschke, R. Monnard, L. Antognini, J. Cattin, A.A. Abdallah, B. Aïssa, M. M. Kivambe, N. Tabet, M. Boccard, C. Ballif, Nanocrystalline silicon oxide stacks for silicon heterojunction solar cells for hot climates, AIP Conf. Proc. 1999 (2018), 30001, https://doi.org/10.1063/1.5049262.
[160] C. Lei, C.-W. Peng, J. Zhong, H. Li, M. Yang, K. Zheng, X. Qu, C. Yu, Y. Li, X. Xu, Phosphorus treatment to promote crystallinity of the microcrystalline silicon front contact layers for highly efficient heterojunction solar cells, Sol. Energy Mater. Sol. Cells 209 (2020), 110439, https://doi.org/10.1016/j.solmat.2020.110439.
[161] S. Nishida, H. Tasaki, M. Konagai, K. Takahashi, Highly conductive and wide band gap amorphous-microcrystalline mixed-phase silicon films prepared by photochemical vapor deposition, J. Appl. Phys. 58 (1985) 1427–1431, https://doi.org/10.1063/1.336071.
[162] A. Wang, G. Lucovsky, Intrinsic microcrystalline silicon deposited by remote PECVD: a new thin-film photovoltaic material, in: IEEE Conf. Photovolt. Spec., IEEE, 1990, pp. 1614–1618, https://doi.org/10.1109/PVSC.1990.111882.
[163] L. Antognini, V. Paratte, J. Haschke, J. Cattin, J. Dréon, M. Lehmann, L.-L. Senaud, Q. Jeangros, C. Ballif, M. Boccard, Influence of the dopant gas precursor in P-type nanocrystalline silicon layers on the performance of front junction heterojunction solar cells, IEEE J. Photovoltaics 11 (2021) 944–956, https://doi.org/10.1109/JPHOTOV.2021.3074072.
[164] A. Richter, L. Zhao, F. Finger, K. Ding, Nano-composite microstructure model for the classification of hydrogenated nanocrystalline silicon oxide thin films, Surf. Coating. Technol. 295 (2016) 119–124, https://doi.org/10.1016/j.surfcoat.2015.09.016.
[165] Y. Xu, Z. Hu, H. Diao, Y. Cai, S. Zhang, X. Zeng, H. Hao, X. Liao, E. Fortunato, R. Martins, Heterojunction solar cells with n-type nanocrystalline silicon emitters on p-type c-Si wafers, J. Non-Cryst. Solids 352 (2006) 1972–1975, https://doi.org/10.1016/j.jnoncrysol.2006.02.028.
[166] J. Sritharathikhun, H. Yamamoto, S. Miyajima, A. Yamada, M. Konagai, Optimization of amorphous silicon oxide buffer layer for high-efficiency p-type hydrogenated microcrystalline silicon oxide/n-type crystalline silicon heterojunction solar cells, Jpn. J. Appl. Phys. 47 (2008) 8452, https://doi.org/10.1143/JJAP.47.8452.
[167] M. Tzolov, F. Finger, R. Carius, P. Hapke, Optical and transport studies on thin microcrystalline silicon films prepared by very high frequency glow discharge for solar cell applications, J. Appl. Phys. 81 (1997) 7376–7385, https://doi.org/10.1063/1.365354.
[168] J. Müllerová, P. Šutta, G. Van Elzakker, M. Zeman, M. Mikula, Microstructure of hydrogenated silicon thin films prepared from silane diluted with hydrogen, Appl. Surf. Sci. 254 (2008) 3690–3695, https://doi.org/10.1016/j.apsusc.2007.10.069.
[169] O. Vetterl, F. Finger, R. Carius, P. Hapke, L. Houben, O. Kluth, A. Lambertz, A. Mück, B. Rech, H. Wagner, Intrinsic microcrystalline silicon: a new material for photovoltaics, Sol. Energy Mater. Sol. Cells 62 (2000) 97–108, https://doi.org/10.1016/S0927-0248(99)00140-3.
[170] M. Stutzmann, D.K. Biegelsen, R.A. Street, Detailed investigation of doping in hydrogenated amorphous silicon and germanium, Phys. Rev. B 35 (1987) 5666, https://doi.org/10.1103/PhysRevB.35.5666.
[171] P. Roca i Cabarrocas, N. Layadi, T. Heitz, B. Drévillon, I. Solomon, Substrate selectivity in the formation of microcrystalline silicon: mechanisms and technological consequences, Appl. Phys. Lett. 66 (1995) 3609–3611, https://doi.org/10.1063/1.113803.
[172] J. Koh, A.S. Ferlauto, P.I. Rovira, C.R. Wronski, R.W. Collins, Evolutionary phase diagrams for plasma-enhanced chemical vapor deposition of silicon thin films from hydrogen-diluted silane, Appl. Phys. Lett. 75 (1999) 2286–2288, https://doi.org/10.1063/1.124992.
[173] L. Mazzarella, S. Kirner, O. Gabriel, S.S. Schmidt, L. Korte, B. Stannowski, B. Rech, R. Schlatmann, Nanocrystalline silicon emitter optimization for Si-HJ solar cells: substrate selectivity and CO2 plasma treatment effect, Phys. Status Solidi Appl. Mater. Sci. 214 (2017), 1532958, https://doi.org/10.1002/pssa.201532958.
[174] A.N. Fioretti, M. Boccard, R. Monnard, C. Ballif, Low-temperature p-type microcrystalline silicon as carrier selective contact for silicon heterojunction solar cells, IEEE J. Photovoltaics 9 (2019) 1158–1165, https://doi.org/10.1109/JPHOTOV.2019.2917550.
[175] J.P. Seif, A. Descoeudres, G. Nogay, S. Hanni, S.M. De Nicolas, N. Holm, J. Geissbuhler, A. Hessler-Wyser, M. Duchamp, R.E. Dunin-Borkowski, M. Ledinsky, S. De Wolf, C. Ballif, Strategies for doped nanocrystalline silicon integration in silicon heterojunction solar cells, IEEE J. Photovoltaics 6 (2016) 1132–1140, https://doi.org/10.1109/JPHOTOV.2016.2571619.
[176] L. Antognini, C. Sthioul, J. Dreon, V. Paratte, D. Tuerkay, L.-L. Senaud, C. Ballif, M. Boccard, Integration of thin n-type nc-Si: H layers in the window-multilayer stack of heterojunction solar cells, Sol. Energy Mater. Sol. Cells 248 (2022), 111975, https://doi.org/10.1016/j.solmat.2022.111975.
[177] L. Mazzarella, A.B. Morales-Vilches, L. Korte, R. Schlatmann, B. Stannowski, Ultra-thin nanocrystalline n-type silicon oxide front contact layers for rear-emitter silicon heterojunction solar cells, Sol. Energy Mater. Sol. Cells 179 (2018) 386–391, https://doi.org/10.1016/j.solmat.2018.01.034.
[178] K.-J. Chang, D.J. Chadi, Theory of hydrogen passivation of shallow-level dopants in crystalline silicon, Phys. Rev. Lett. 60 (1988) 1422, https://doi.org/10.1103/PhysRevLett.60.1422.
[179] N.M. Johnson, C. Herring, D.J. Chadi, Interstitial hydrogen and neutralization of shallow-donor impurities in single-crystal silicon, Phys. Rev. Lett. 56 (1986) 769, https://doi.org/10.1103/PhysRevLett.56.769.
[180] K. Bergman, M. Stavola, S.J. Pearton, J. Lopata, Donor-hydrogen complexes in passivated silicon, Phys. Rev. B 37 (1988) 2770, https://doi.org/10.1103/PhysRevB.37.2770.
[181] P. Roca i Cabarrocas, N. Layadi, B. Drevillon, I. Solomon, Microcrystalline silicon growth by the layer-by-layer technique: long term evolution and nucleation mechanisms, J. Non-Cryst. Solids 198–200 (1996) 871–874, https://doi.org/10.1016/0022-3093(96)00073-7.
[182] N. Layadi, P.R. i Cabarrocas, B. Drévillon, I. Solomon, Real-time spectroscopic ellipsometry study of the growth of amorphous and microcrystalline silicon thin films prepared by alternating silicon deposition and hydrogen plasma treatment, Phys. Rev. B 52 (1995) 5136, https://doi.org/10.1103/PhysRevB.52.5136.
[183] A. Matsuda, Formation kinetics and control of microcrystallite in μc-Si:H from glow discharge plasma, J. Non-Cryst. Solids 59–60 (1983) 767–774, https://doi.org/10.1016/0022-3093(83)90284-3.

[184] J.E. Gerbi, J.R. Abelson, Deposition of microcrystalline silicon: direct evidence for hydrogen-induced surface mobility of Si adspecies, J. Appl. Phys. 89 (2001) 1463–1469, https://doi.org/10.1063/1.1334639.
[185] Y. Zhao, P. Procel, C. Han, L. Mazzarella, G. Yang, A. Weeber, M. Zeman, O. Isabella, Design and optimization of hole collectors based on nc-SiOx: H for high-efficiency silicon heterojunction solar cells, Sol. Energy Mater. Sol. Cells 219 (2021), 110779, https://doi.org/10.1016/j.solmat.2020.110779.
[186] Z.C. Holman, A. Descoeudres, L. Barraud, F.Z. Fernandez, J.P. Seif, S. De Wolf, C. Ballif, Current losses at the front of silicon heterojunction solar cells, IEEE J. Photovoltaics 2 (2012) 7–15, https://doi.org/10.1109/JPHOTOV.2011.2174967.
[187] P. Gao, Z. Yang, J. He, J. Yu, P. Liu, J. Zhu, Z. Ge, J. Ye, Dopant-free and carrier-selective heterocontacts for silicon solar cells: recent advances and perspectives, Adv. Sci. 5 (2018), 1700547, https://doi.org/10.1002/advs.201700547.
[188] L.G. Gerling, S. Mahato, A. Morales-Vilches, G. Masmitja, P. Ortega, C. Voz, R. Alcubilla, J. Puigdollers, Transition metal oxides as hole-selective contacts in silicon heterojunctions solar cells, Sol. Energy Mater. Sol. Cells 145 (2016) 109–115, https://doi.org/10.1016/j.solmat.2015.08.028.
[189] L. Mazzarella, A. Alcañiz, P. Procel, E. Kawa, Y. Zhao, U. Tiringer, C. Han, G. Yang, P. Taheri, M. Zeman, O. Isabella, Strategy to mitigate the dipole interfacial states in (i) a-Si: H/MoOx passivating contacts solar cells, Prog. Photovoltaics Res. Appl. 29 (2021) 391–400, https://doi.org/10.1002/pip.3381.
[190] J.E. Medvedeva, Combining optical transparency with electrical conductivity: challenges and prospects, Transparent Electron, From Synth. to Appl. 29 (2010), https://doi.org/10.1002/9780470710609.ch1.
[191] K.L. Chopra, S. Major, D.K. Pandya, Transparent conductors—a status review, Thin Solid Films 102 (1983) 1–46, https://doi.org/10.1016/0040-6090(83)90256-0.
[192] M. Morales-masis, S. De Wolf, R. Woods-robinson, J.W. Ager, C. Ballif, Transparent Electrodes for Efficient Optoelectronics 3 (2017), 1600529, https://doi.org/10.1002/aelm.201600529.
[193] C. Han, Y. Zhao, L. Mazzarella, R. Santbergen, A. Montes, P. Procel, G. Yang, X. Zhang, M. Zeman, O. Isabella, Room-temperature sputtered tungsten-doped indium oxide for improved current in silicon heterojunction solar cells, Sol. Energy Mater. Sol. Cells 227 (2021), 111082, https://doi.org/10.1016/j.solmat.2021.111082.
[194] C. Han, L. Mazzarella, Y. Zhao, G. Yang, P. Procel, M. Tijssen, A. Montes, L. Spitaleri, A. Gulino, X. Zhang, O. Isabella, M. Zeman, High-mobility hydrogenated fluorine-doped indium oxide film for passivating contacts c-Si solar cells, ACS Appl. Mater. Interfaces 11 (2019) 45586–45595, https://doi.org/10.1021/acsami.9b14709.
[195] C. Han, R. Santbergen, M. van Duffelen, P. Procel, Y. Zhao, G. Yang, X. Zhang, M. Zeman, L. Mazzarella, O. Isabella, Towards bifacial silicon heterojunction solar cells with reduced TCO use, Prog. Photovoltaics Res. Appl. 30 (2022) 750–762, https://doi.org/10.1002/pip.3550.
[196] A. Alcañiz Moya, Numerical Simulation of C-Si Solar Cells Based on Transition Metal Oxide as Carrier Selective Contact: Drift Diffusion and Ab Initio, Delft University of Technology, 2020. http://resolver.tudelft.nl/uuid:e1537b2c-d106-415e-9762-2664146790c6.
[197] A. Cruz, F. Ruske, A. Eljarrat, P.P. Michalowski, A.B. Morales-Vilches, S. Neubert, E.-C. Wang, C.T. Koch, B. Szyszka, R. Schlatmann, B. Stannowski, Influence of silicon layers on the growth of ITO and AZO in silicon heterojunction solar cells, IEEE J. Photovoltaics 10 (2019) 703–709, https://doi.org/10.1109/JPHOTOV.2019.2957665.
[198] K.-U. Ritzau, T. Behrendt, D. Palaferri, M. Bivour, M. Hermle, Hydrogen doping of Indium Tin Oxide due to thermal treatment of hetero-junction solar cells, Thin Solid Films 599 (2016) 161–165, https://doi.org/10.1016/j.tsf.2015.12.027.
[199] C. Han, G. Yang, A. Montes, P. Procel, L. Mazzarella, Y. Zhao, S. Eijt, H. Schut, X. Zhang, M. Zeman, O. Isabella, Realizing the potential of RF-sputtered hydrogenated fluorine-doped indium oxide as an electrode material for ultrathin SiOx/poly-Si passivating contacts, ACS Appl. Energy Mater. 3 (2020), https://doi.org/10.1021/acsaem.0c01206.
[200] J. Haschke, G. Christmann, C. Messmer, M. Bivour, M. Boccard, C. Ballif, Lateral transport in silicon solar cells, J. Appl. Phys. 127 (2020), 114501, https://doi.org/10.1063/1.5139416.
[201] Fraunhofer Institute for Solar Energy Systems, Innovative Fine-Line Screen Printing Metallization Reduces Silver Consumption for Solar Cell Contacts, 2019. https://www.ise.fraunhofer.de/en/press-media/press-releases/2019/innovative-fine-line-screen-printing-metallization-reduces-silver-consumption-for-solar-cell-contacts.html. (Accessed 20 February 2012).
[202] G. Limodio, Y. De Groot, G. Van Kuler, L. Mazzarella, Y. Zhao, P. Procel, G. Yang, O. Isabella, M. Zeman, Copper-plating metallization with alternative seed layers for c-Si solar cells embedding carrier-selective passivating contacts, IEEE J. Photovoltaics 10 (2019) 372–382, https://doi.org/10.1109/JPHOTOV.2019.2957671.
[203] C. Han, G. Yang, P. Procel, D. O'Connor, Y. Zhao, A. Gopalakrishnan, X. Zhang, M. Zeman, L. Mazzarella, O. Isabella, Controllable simultaneous bifacial Cu-plating for high efficiency crystalline silicon solar cells, Sol. RRL. 6 (2022), 2100810, https://doi.org/10.1002/solr.202100810.
[204] I. Shoukry, J. Libal, R. Kopecek, E. Wefringhaus, J. Werner, Modelling of bifacial gain for stand-alone and in-field installed bifacial PV modules, Energy Proc. 92 (2016) 600–608, https://doi.org/10.1016/j.egypro.2016.07.025.
[205] X. Sun, M.R. Khan, C. Deline, M.A. Alam, Optimization and performance of bifacial solar modules: a global perspective, Appl. Energy 212 (2018) 1601–1610, https://doi.org/10.1016/j.apenergy.2017.12.041.
[206] D. Zhang, I.A. Digdaya, R. Santbergen, R. Van Swaaij, P. Bronsveld, M. Zeman, J. A.M. Van Roosmalen, A.W. Weeber, Design and fabrication of a SiOx/ITO double-layer anti-reflective coating for heterojunction silicon solar cells, Sol. Energy Mater. Sol. Cells 117 (2013) 132–138, https://doi.org/10.1016/j.solmat.2013.05.044.
[207] H. Fujiwara, R.W. Collins, Spectroscopic Ellipsometry for Photovoltaics, Springer, 2018, https://doi.org/10.1007/978-3-319-75377-5.
[208] Z.C. Holman, M. Filipič, A. Descoeudres, S. De Wolf, F. Smole, M. Topič, C. Ballif, Infrared light management in high-efficiency silicon heterojunction and rear-passivated solar cells, J. Appl. Phys. 113 (2013), 013107, https://doi.org/10.1063/1.4772975.
[209] Y. Zhao, L. Mazzarella, P. Procel Moya, O. Isabella, M. Zeman, Electron Transport Layer- And/or Hole Transport Layer-free Silicon Heterojunction Solar Cells, NL2028691B1; WO2023/287279A1, 2021.
[210] P. Procel Moya, G. Yang, M. Zeman, O. Isabella, L. Mazzarella, Transparent Passivated Contacts for Si Solar Cells, NL2024024B1; EP4046205A1; WO2021075956A1, 2019.
[211] P. Procel Moya, O. Isabella, Localized Passivated Contacts for Solar Cells, P100803NL00, 2022.
[212] A. Klein, C. Körber, A. Wachau, F. Säuberlich, Y. Gassenbauer, S.P. Harvey, D. E. Proffit, T.O. Mason, Transparent conducting oxides for photovoltaics: manipulation of fermi level, work function and energy band alignment, Materials 3 (2010) 4892–4914, https://doi.org/10.3390/ma3114892.
[213] Y. Smirnov, L. Schmengler, R. Kuik, P. Repecaud, M. Najafi, D. Zhang, M. Theelen, E. Aydin, S. Veenstra, S. De Wolf, Scalable pulsed laser deposition of transparent rear electrode for perovskite solar cells, Adv. Mater. Technol. 6 (2021), 2000856, https://doi.org/10.1002/admt.202000856.
[214] Z. Lu, F. Meng, Y. Cui, J. Shi, Z. Feng, Z. Liu, High quality of IWO films prepared at room temperature by reactive plasma deposition for photovoltaic devices, J. Phys. D Appl. Phys. 46 (2013), 75103, https://doi.org/10.1088/0022-3727/46/7/075103.
[215] H. Liu, Y. Gong, H. Diao, X. Jia, L. Zhao, W. Wang, W. Wang, J. Zong, Comparative study on IWO and ICO transparent conductive oxide films prepared by reactive plasma deposition for copper electroplated silicon heterojunction solar cell, J. Mater. Sci. Mater. Electron. 33 (2022) 5000–5008, https://doi.org/10.1007/s10854-021-07689-2.
[216] H. Steinkemper, F. Feldmann, M. Bivour, M. Hermle, Numerical simulation of carrier-selective electron contacts featuring tunnel oxides, IEEE J. Photovoltaics 5 (2015) 1348–1356, https://doi.org/10.1109/JPHOTOV.2015.2455346.
[217] P. Procel, G. Yang, O. Isabella, M. Zeman, Numerical simulations of IBC solar cells based on poly-Si carrier-selective passivating contacts, IEEE J. Photovoltaics 9 (2019) 374–384, https://doi.org/10.1109/JPHOTOV.2019.2892527.
[218] P. Procel, P. Löper, F. Crupi, C. Ballif, A. Ingenito, Numerical simulations of hole carrier selective contacts in p-type c-Si solar cells, Sol. Energy Mater. Sol. Cells 200 (2019), 109937, https://doi.org/10.1016/j.solmat.2019.109937.